Mechanistic Studies of an Automated Lipid Nanoparticle Reveal Critical Pharmaceutical Properties Associated with Enhanced mRNA Functional Delivery In Vitro and In Vivo

Lili Cui,* Morag R. Hunter, Silvia Sonzini, Sara Pereira, Steven M. Romanelli, Kai Liu, Weimin Li, Lihuan Liang, Bin Yang, Najet Mahmoudi, and Arpan S. Desai

Recently, lipid nanoparticles (LNPs) have attracted attention due to their emergent use for COVID-19 mRNA vaccines. The success of LNPs can be attributed to ionizable lipids, which enable functional intracellular delivery. Previously, the authors established an automated high-throughput platform to screen ionizable lipids and identified that the LNPs generated using this automated technique show comparable or increased mRNA functional delivery in vitro as compared to LNPs prepared using traditional microfluidics techniques. In this study, the authors choose one benchmark lipid, DLin-MC3-DMA (MC3), and investigate whether the automated formulation technique can enhance mRNA functional delivery in vivo. Interestingly, a 4.5-fold improvement in mRNA functional delivery in vivo by automated LNPs as compared to LNPs formulated by conventional microfluidics techniques, is observed. Mechanistic studies reveal that particles with large size accommodate more mRNA per LNP, possess more hydrophobic surface, are more hemolytic, bind a larger protein corona, and tend to accumulate more in macropinocytosomes, which may quantitatively benefit mRNA cytosolic delivery. These data suggest that mRNA loading per particle is a critical factor that accounts for the enhanced mRNA functional delivery of automated LNPs. These mechanistic findings provide valuable insight underlying the enhanced mRNA functional delivery to accelerate future mRNA LNP product development.

1. Introduction

Messenger RNA (mRNA) as an emerging new therapeutic modality has gathered worldwide attention due to the COVID-19 pandemic and the emergence of mRNA-based vaccines. Compared to traditional vaccines, mRNA-based vaccines offer several advantages. First, mRNA-based therapies are taken up by cells and transiently expressed to their encoded protein in the cytosol, bypassing the requirement to enter the nucleus. Additionally, mRNA can be generated in multi-gram scale via a robust and cost-effective in vitro transcription approach.[1–3] These features make mRNA an excellent candidate for fast vaccine clinical development.[3,4] Of the current FDA-approved COVID-19 vaccines for emergency use, two of them are mRNA-based.[5] mRNA also has other therapeutic applications as in cancer immunology, protein replacement, gene editing, and ex vivo therapy.[6–10] Despite the above advantages, mRNA is immunogenic, sensitive to RNases, and usually

L. Cui, M. R. Hunter, S. Sonzini, S. Pereira, W. Li, B. Yang, A. S. Desai
Advanced Drug Delivery
Pharmaceutical Sciences
BioPharmaceuticals R&D
AstraZeneca, Cambridge CB21 6GH, UK
E-mail: lili.cui@astrazeneca.com; lilicuinike@gmail.com
S. M. Romanelli
University of Michigan Medical School
Department of Molecular & Integrative Physiology
Ann Arbor, MI 48109-5624, USA
K. Liu
Advanced Drug Delivery
Pharmaceutical Sciences
BioPharmaceuticals R&D
AstraZeneca, Gothenburg 43183, Sweden

L. Liang
Bioscience Renal
Research and Early Development
Cardiovascular
Renal & Metabolism (CVRM)
BioPharmaceuticals R&D
AstraZeneca, Cambridge CB21 6GH, UK
N. Mahmoudi
Rutherford Appleton Laboratory
ISIS Facility
Science and Technology Facilities Council
Didcot OX11 0QX, UK

**ADVANCED
SCIENCE NEWS**
www.advancedsciencenews.com

NANO · MICRO
small
www.small-journal.com

has a short half-life.[11–13] Current strategies to reduce undesired immunogenicity and increase mRNA stability include mRNA chemical modification.[14–16] Besides, efforts to enhance mRNA delivery using novel delivery vehicles have been attempted, but further understanding is required to optimize these delivery strategies.[4,9,17,18]

To this end, lipid nanoparticles (LNPs) represent the most successful non-viral delivery technology for mRNA. LNPs encapsulate mRNA in their core, shielding it from degradation by RNAses. The encapsulation ability is facilitated by the composition of the LNPs, which is comprised of ionizable lipids, structural lipids, and steric lipids. Of these components, the ionizable lipid is considered the most critical factor, as its structure enables endosomal escape which is considered to be a rate limiting step for intracellular delivery.[19,20] For example, the ionizable lipid DLin-MC3-DMA (MC3), has an inverted cone shape geometry due to its small head group and bulky tails, which allows it to adopt a negative curvature and form a reverse hexagonal micellular structure upon protonation within the endosome.[21] This disrupts the endosomal membrane, and allows the mRNA cargo to escape into the cytosol for protein translation.[21] As such, research on LNP formulation has focused on developing ionizable lipids with improved structural features to enhance mRNA functional delivery.[22] Additionally, ionizable lipids must be biodegradable and safe, as highlighted by several LNPs that failed clinical trials owing to lack of efficacy and unfavorable safety profiles.[23,24] Thus, identifying candidate ionizable lipids requires screening libraries of hundreds to thousands of new structures.[25–27]

In addition to structural improvements, LNP research has also focused on improving the entry of LNPs to tissues or cells of interest. Currently, there is a lack of understanding of how the physiochemical properties of LNPs influence their interactions with biological systems and contribute to functional mRNA delivery. For example, LNP morphology may play a critical role, as lamellar structures have been shown to enhance intracellular mRNA expression as compared to spherical LNP structures.[28–31] For in vivo delivery, factors such as pKa and surface charge of LNPs have been shown to play important roles in the formation of the protein corona, which influences tissue distribution and mRNA delivery efficiency.[9,32,33] Thus, developing efficient LNPs for enhanced functional mRNA delivery requires a deep understanding of all of these factors.

To accelerate the study of LNPs, we previously developed an automated high-throughput platform to integrate formulation preparation, biophysical characterization, and biological evaluation of LNPs encapsulating mRNA.[34] This platform enables generation of hundreds or thousands of LNPs in a time- and cost-effective manner and can be applied to screen mRNA LNPs made from novel ionizable lipids in vitro.[34] It is acknowledged that the development of novel ionizable lipids with improved chemical structures represents a main delivery challenge as it requires the design of large lipid libraries which must be screened for delivery efficiency.[25,26,35] Indeed, using our automated high-throughput mRNA LNP formulation technique, we demonstrated that a library of novel LNPs could be rapidly generated and screened compared to traditional microfluidics techniques.[34] We also surprisingly found that this automated technique imparted enhanced mRNA functional

delivery over traditional microfluidics devices despite using the same lipid compositions.[34] In the current study, we sought to further investigate the mechanistic and physiochemical properties of LNPs prepared using this automated process. Additionally, we explored LNP-mediated mRNA delivery efficiency both in vitro and in vivo and found that LNPs formulated using the automated technique had a 4.5-fold improvement in mRNA functional delivery in vivo as compared to LNPs formulated using traditional techniques. Ultimately, this study emphasizes the impact of LNP physicochemical properties on the in vitro and in vivo mRNA functional delivery to accelerate their use for therapeutic applications.

2. Results and Discussion

2.1. Automated LNPs Enhance mRNA Functional Delivery to Different Cell Lines

Previously, we established an automated high-throughput platform for screening LNPs for mRNA delivery.[34] This automated high-throughput platform is based on a common lab-used liquid handling system and features fast and cost-effective preparation, characterization, and in vitro evaluation of hundreds or thousands of mRNA LNPs. We have shown that LNPs made from the automated high-throughput platform exhibited comparable or higher mRNA delivery efficiency than the LNPs generated from a standard microfluidic mixing platform.[34] This interesting finding motivated an investigation into whether the enhanced delivery profile persists for other mRNA cargoes and in other cell types. We chose DLin-MC3-DMA (MC3) for this study as it is the current "benchmark" ionizable lipid species used in LNP products and publications.[20,36,37] In previous studies, we encapsulated mRNA encoding eGFP, however, in this study, we incorporated mRNA encoding mCherry and evaluated the functional delivery profile in H358, HepG2, and HEK293T cells as illustrated in **Figure 1**. Interestingly, LNPs generated using the automated platform (automated LNPs) possessed a fourfold ($p < 0.001$) increase in mCherry expression in H358 cells at a dose of 50 ng mRNA per well as compared to LNPs generated using the standard technique (standard LNPs) (Figure 1a). We also observed a dose-dependent increase in mCherry expression across HepG2 (3.5-fold) and HEK293T (370-fold) cells transfected with automated LNPs, thereby demonstrating consistency across different cell types (Figure 1b,c).

2.2. Morphological Characterization of Automated and Standard mRNA LNPs by DLS and CryoTEM

To probe the morphological characteristics of automated and standard mRNA LNPs, we measured their hydrodynamic size using dynamic light scattering (DLS) (**Figure 2**a). As expected, both platforms generated nanoparticles with a single intensity and number distribution peak indicating one particle population (Figure 2a). However, the hydrodynamic size of the automated mRNA LNPs was larger than that of the standard mRNA LNPs. Additionally, the automated mRNA LNPs had a slightly higher polydispersity index (PDI) (**Table 1**) as compared to the
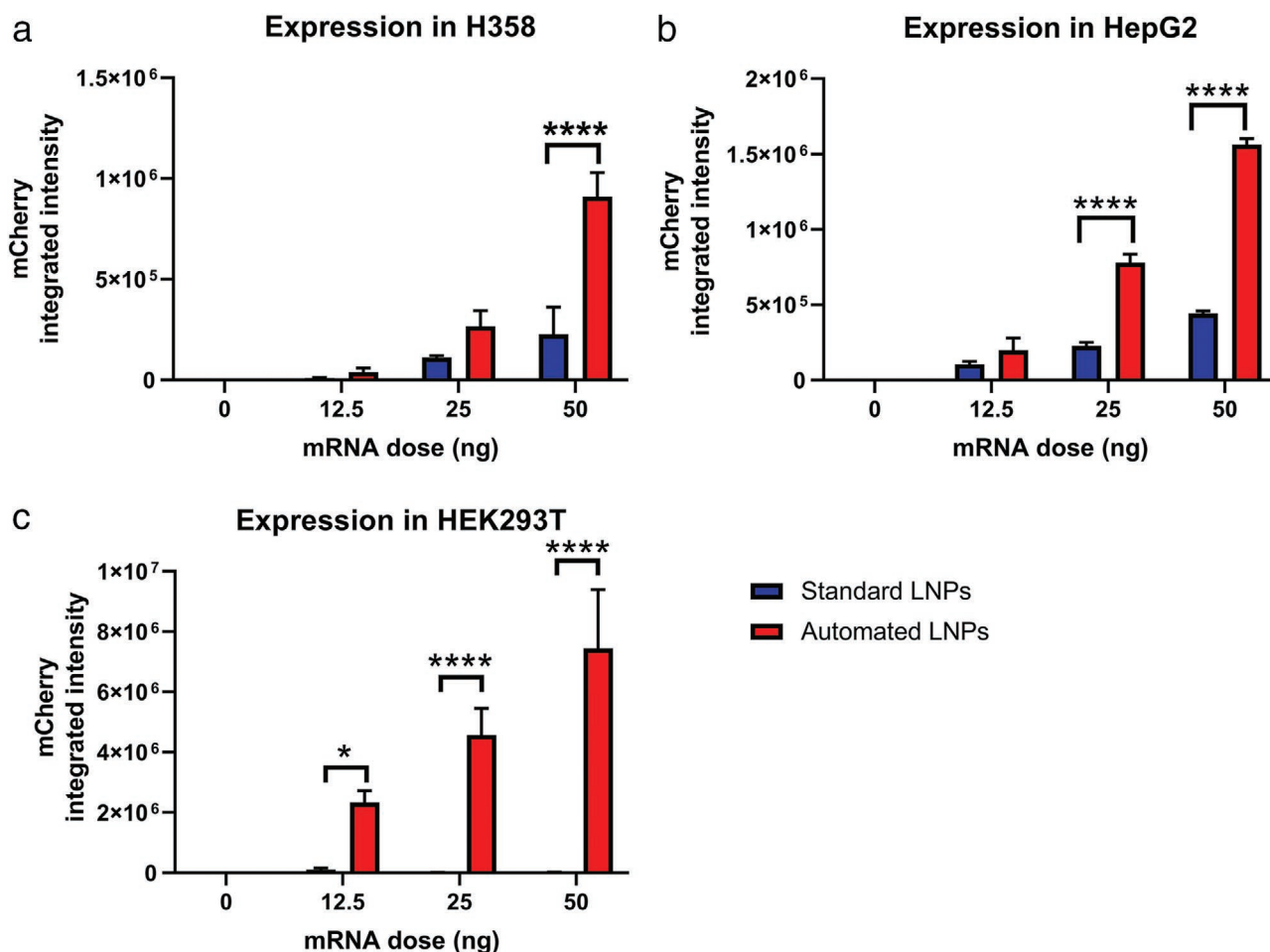
Figure 1. Functional delivery of automated and standard LNPs loaded with mCherry mRNA at different doses in a) H358, b) HepG2, and c) HEK293T cell lines. Two-way ANOVA analysis followed by Tukey's multiple comparisons. *$p < 0.05$; ****$p < 0.0001$.

standard mRNA LNPs. We observed a similar trend in our previous studies, which is likely attributed to the lack of mixing microstructures in the automated LNP formulation process.[34] In another study, we designed a group of large mRNA LNPs (≈120 nm) and a group of small mRNA LNPs (≈70 nm), which had the same composition and ratios, but were formulated using different mixing flow rates and volume ratios.[38] The size set below 200 nm is to enable sterile filtration via 0.20 or 0.22 µm pore membrane since sterilization is a key attribute of parenteral formulations.[39] Within the formulation groups, the percentage of DSPC and cholesterol lipids varied while that of MC3 and PEG lipids was kept constant. Surprisingly, all the large particles exhibited higher mCherry mRNA expression in H358 cells than the small particles regardless of formulation composition ratios, suggesting that particle size is correlated with mRNA functional delivery.[38]

Next, we further probed the morphology of both mRNA LNP formulations using cryogenic transmission electron microscopy (cryoTEM) (Figure 2b). For direct comparison, both automated and standard mRNA LNPs were prepared and processed in parallel for imaging. As shown in Figure 2b, the standard mRNA LNPs exhibited spherical particles with an electron dense core. Interestingly, the automated mRNA LNPs also exhibited an electron dense spherical shape, but were slightly more polydisperse in terms of size, which was consistent with the results from DLS (Figure 2a). The size from DLS is generally larger than that from cryoTEM due to the presence of the hydration layer around particles in Brownian motion.[29] DLS is sensitive to the presence of large particles and indeed, large mRNA LNPs were observed in cryoTEM (Figure S1, Supporting Information). Additionally, we observed that the automated mRNA LNPs localized in the carbon film support whereas the standard mRNA LNPs were distributed across the ice holes (Figure 2b). Considering both mRNA LNPs are relatively neutral (ζ-potential in Table 1), this difference in localization may suggest that the surface of the automated mRNA LNPs is more hydrophobic.

2.3. Structural Characterization of Automated and Standard mRNA LNPs by SANS/SAXS

To investigate the internal structure of automated and standard mRNA LNPs, we utilized small angle neutron scattering (SANS) and small angle X-ray scattering (SAXS) (**Figure 3**a,b). The contrast required for SANS and SAXS detection comes from the difference in scattering length density (SLD) between
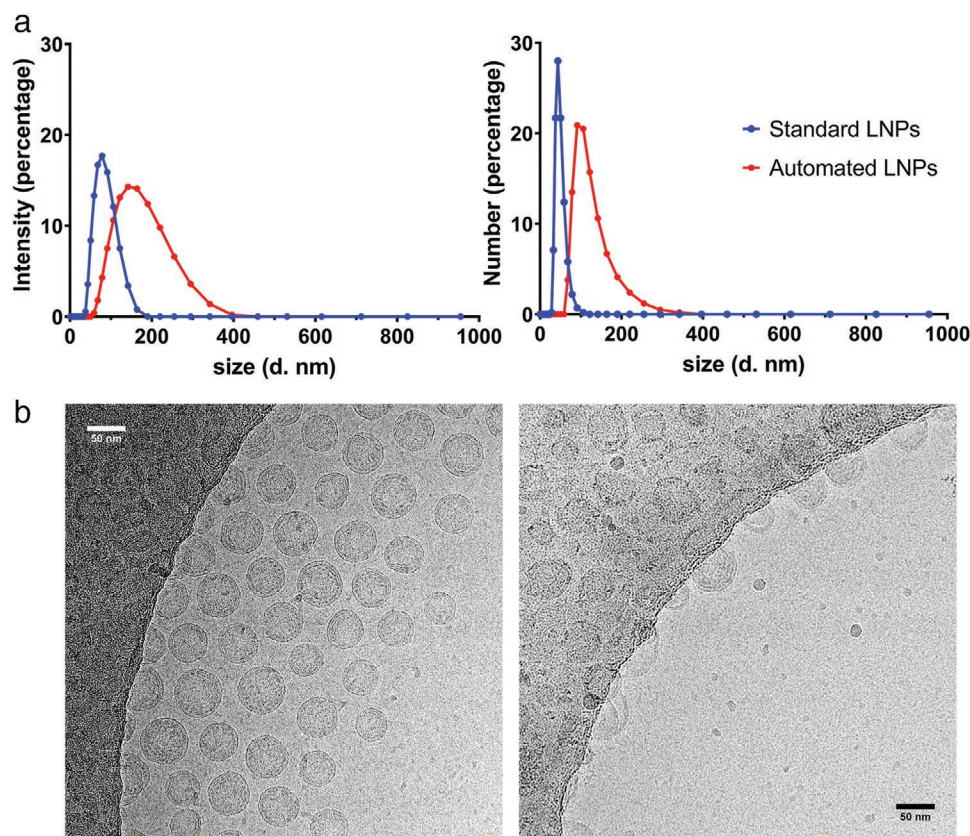
Figure 2. Morphological characterization of automated and standard mRNA LNPs. a) Hydrodynamic intensity and number size distribution by DLS. b) mRNA LNP morphology visualized by cryoTEM.

LNP components and solvent. In general, SANS varies by scattering length of the nucleus whereas SAXS varies in proportion to electron density. Therefore, the two techniques can be used in tandem to measure the scattering profiles of each mRNA LNP to model their internal structures.

The DSPC and cholesterol components used in the mRNA LNP formulations are deuterated while the solvent contains 27% D_2O and 73% H_2O (volume ratios). This condition renders a featured peak (a bump at a Q value of ≈0.1 nm^{-1}) visible for the standard LNPs.[29] To note, both the standard mRNA LNPs and the automated mRNA LNPs have the same lipid components and ratios. As expected, the scattering intensity of the standard mRNA LNPs increased from high Q to low Q and showed a featured peak at 0.1 nm^{-1}, consistent with previous observations.[29] In contrast, there is no featured peak visible for the automated mRNA LNPs indicating a wide size distribution.

In line with the principle of using a small number of free parameters to fit the scattering curve, a model of a polydisperse core with two shells was applied (as depicted in Figure 3a). In

this model, the core of the mRNA LNPs is composed of the majority of MC3 and cholesterol, mRNA, and solvent. Surrounding the core are two shells. Shell 1 contains mainly DSPC and a small portion of MC3 and cholesterol as well as the hydrophobic part of DMG-PEG lipids. By contrast, shell 2 is a hydrophilic layer of PEG. The resultant fitting of the SANS and SAXS data for the two mRNA LNPs is shown in solid lines in Figure 3. A global fitting of SANS and SAXS data for either standard LNPs or the automated mRNA LNPs is shown in Figure S2, Supporting Information. The best fitted parameters using polydisperse core with two shells model is shown in Table S1, Supporting Information. Of the key fitted parameters summarized in **Table 2**, the standard mRNA LNPs has a core of 19.16 nm in radius, a shell 1 of 1.96 nm, and a shell 2 of 4.12 nm, consistent with the previous studies.[29] These values give the diameter of the standard mRNA LNPs at 50.5 nm which corresponds well with the particle size observed in cryoTEM images (Figure 2). In comparison, the core of the automated mRNA LNPs is 22.45 nm in radius while shell 1 and

Table 1. Summary of physicochemical properties of eGFP mRNA LNPs.

LNPs	ζ-size [nm]	PDI	ζ [mV]	EE [%]
Standard	72.9 ± 5.7	0.095 ± 0.035	3.98	96.1 ± 1.7
Automated	147.4 ± 9.2	0.125 ± 0.028	3.13	74.4 ± 4.9

$n = 10$ for size, PDI, and mRNA encapsulation efficiency (EE%).

ADVANCED
SCIENCE NEWS
www.advancedsciencenews.com
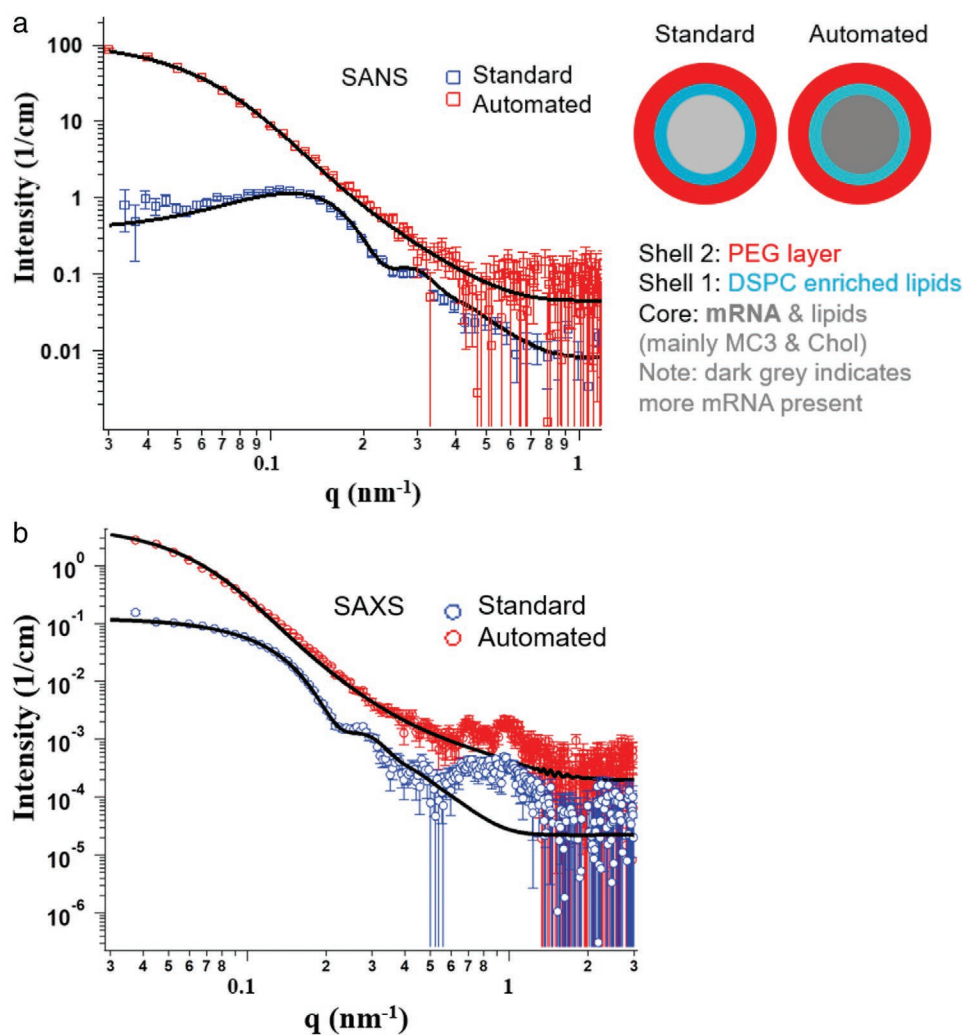
NANO · MICRO
small
www.small-journal.com

Figure 3. Structural characterization of mRNA LNPs using a) SANS and b) SAXS. The solid lines represent the best fitting using polydisperse core with two shells model.

shell 2 are 2.32 and 4.10 nm, giving a total diameter of 57.7 nm. It is worth noting that we pursued to fit the scattering data of the automated mRNA LNPs using a core radius of 30–50 nm (as calculated from number size in the DLS measurement in Figure 2a). However, the curve didn't fit when the core radius was increasing. Particle size from SANS is normally smaller than that from DLS since SANS uses the mRNA LNP SLD difference from solvent as a contrast while DLS is based on LNP Brownian motion (hydrodynamic size with solvent layers). Interestingly, the major difference between the two mRNA LNPs is the thickness of shell 1 and the resultant volume (Table 2). The shell 1 volume for the automated mRNA LNPs is 1.6-fold of that for the standard mRNA LNPs revealing a more hydrophobic layer on the surface. The more hydrophobic surface of the automated mRNA LNPs is consistent with the tendency to distribute toward carbon film and supports the presence of bilayer "bleb" structures observed in the cryoTEM image (Figure 2b; Figure S1, Supporting Information). It is reported that the bilayer "bleb" structures come from bilayer-forming lipids segregating from LNP nanoparticles.[28] Moreover, the hydrophobic surface

of the automated mRNA LNPs is correlated with their enhanced mRNA functional delivery as evidenced by our previous observation that standard mRNA LNPs exhibited higher mRNA expression when DSPC on the surface increased from 0.4 to 0.9 molecule per nm².[38] This also agrees with another report that mRNA expression was improved when DSPC percentage in the LNP formulations increased from 10% to 16%.[40]

Another interesting finding is that the automated mRNA LNPs have a higher SLD value in the core than the standard mRNA LNPs (2.30 E⁻⁴ vs 1.80 E⁻⁴ nm⁻² for SANS and 9.81 E⁻⁴ vs 9.42 E⁻⁴ nm⁻² for SAXS, Table S1, Supporting Information). It indicates that there is a higher amount of components in the core of the automated mRNA LNPs. The SLD value of each component used in the fitting is shown in Table S2, Supporting Information. It contains the calculated SLD of the solvent (27% D₂O + 73% H₂O) and SLD of the lipids (MC3 + Chol) specific for the core according to,

$$SLD(total) = \sum_{1}^{i} SLD * vf \tag{1}$$

ADVANCED
SCIENCE NEWS
www.advancedsciencenews.com

NANO · MICRO
small
www.small-journal.com

Table 2. Structure information of mRNA-LNPs obtained from the best fit of SANS/SAXS data using polydisperse core with two shells model.

Fitted parameters	SANS standard	SANS automated	SAXS standard	SAXS automated
Core radius [nm]	19.16 ± 0.03	22.45 ± 0.07	19.16 ± 0.03	22.45 ± 0.07
Shell 1 thickness [nm]	1.96 ± 0.08	2.32 ± 0.02	1.96 ± 0.08	2.32 ± 0.02
Shell 2 thickness [nm]	4.12 ± 0.02	4.10 ± 0.02	4.12 ± 0.02	4.10 ± 0.02
Core volume [nm³]	29 462	47 394	29 462	47 394
Shell 1 volume [nm³]	9998	16 264	9998	16 264
Shell 2 volume [nm³]	27 891	37 132	27 891	37 132
Volume faction of mRNA in the core (SAXS)	–	–	0.154	0.210
Volume fraction of MC3, chol, water (SAXS)	–	–	0.845	0.789
Volume fraction of MC3, chol (SANS)	0.566	0.409	–	–
Water fraction in the core (combine SANS and SAXS)	–	–	0.279	0.380

Where vf is the volume fraction of each component. The difference in neutron contrast between the LNP core components (mRNA > solvent >lipids) and their interactions make the core visible for SANS as two parts: part one is seen as mRNA in solvent (with high SLD) and part two is visible as lipids (MC3 + chol) (with low SLD). With the above equation and the input formulation molar ratio, the volume fraction of the aqueous materials (mRNA + solvent) and that of the lipids (MC3 + chol) in the core can be obtained (Table 2). We found 56.6% of the core is MC3 and cholesterol for the standard LNPs and 40.9% for the automated LNPs. It implies that there is 43.4% and 59.1% of mRNA plus solvent in the core of the standard LNPs and the automated LNPs, respectively. These values are in the reported range for mRNA and solvent fractions in the core of similar LNPs.[29,41] Considering that the automated LNPs have a higher fraction of mRNA and solvent and the automated LNPs are repeatedly more potent than the standard LNPs, it is not unreasonable to predict that mRNA fraction in the core of the automated LNPs is higher. To note, the core polydispersity of the automated mRNA LNPs is much higher than the standard mRNA LNPs (0.402 vs 0.162) (Table S1, Supporting Information), consistent with the broad scattering pattern in the low Q range ($\approx$0.1 nm^{-1}). The higher dispersity of the automated mRNA LNPs was also observed in the DLS measurement (Figure 2) and cryoTEM image (Figure S1, Supporting Information).

Next, we investigated the higher core SLD for the automated mRNA LNPs fitted from the SAXS data (Table S1, Supporting Information). The SAXS SLD of the solvent is close to that of the lipids but is much lower than that of mRNA present in the core (Table S2, Supporting Information). This suggests that the scattering contrast in SAXS measurements is between two parts, part one containing MC3 + chol + solvent, and part two including the mRNA. Therefore, the mRNA volume fraction in the core can be obtained from SAXS fitting parameters via the SLD equation presented above. As shown in Table 2, the automated LNPs contain 21.0% mRNA while the standard LNPs have 15.4% mRNA per particle. The higher mRNA loading

per particle in the automated LNPs (1.4-fold) is consistent with their enhanced functional delivery of mRNA, which is constantly seen across cell types (Figure 1). Extracting the volume fraction of mRNA from the total volume fraction of mRNA + solvent obtained from SANS fitting data, we found 38.0% and 27.9% solvent fraction for the automated mRNA LNPs and the standard mRNA LNPs, respectively. Previous reports found the fraction of solvent is in the range of 13–24% for standard LNPs[29,41] and the solvent increases when a higher amount of mRNA is present in the core.

It is worthwhile to note that the scattering profiles of the two mRNA LNPs in the high Q range (0.5–3 nm^{-1}) tend to be varied, which indicates different internal structures in the core. Automated mRNA LNPs have two peaks at $\approx$0.7 and 0.9 nm^{-1} (corresponding to d-spacing of 8.9 and 6.9 nm, respectively) which may indicate the presence of a bi-continuous cubic (pn3m) phase. In contrast, the broad peak in the standard mRNA LNPs with an internal d-spacing of 8 nm might represent a characteristic d-spacing of the inverse worm-like micelles structure, which was seen previously.[29] The internal structure of LNPs was affected by the presence or absence of mRNA[29] which is an indirect indication of the amount of mRNA present. Further studies are needed to deconvolute the detailed core structure of mRNA LNPs.

2.4. Macropinosomal Uptake Contributes to Enhanced mRNA Functional Delivery of Automated LNPs

To characterize the cellular uptake process and kinetics of automated and standard mRNA LNPs, Cy5-labeled mRNA was encapsulated in each LNP formulation and transfected into H358 cells. We used confocal microscopy to monitor expression kinetics at 30, 60, and 120 min post transfection (**Figure** 4a). Figure 4b illustrates quantification of Cy5-labeled mRNA cellular uptake at each respective time point. We observed that both automated and standard mRNA LNPs were shown to be
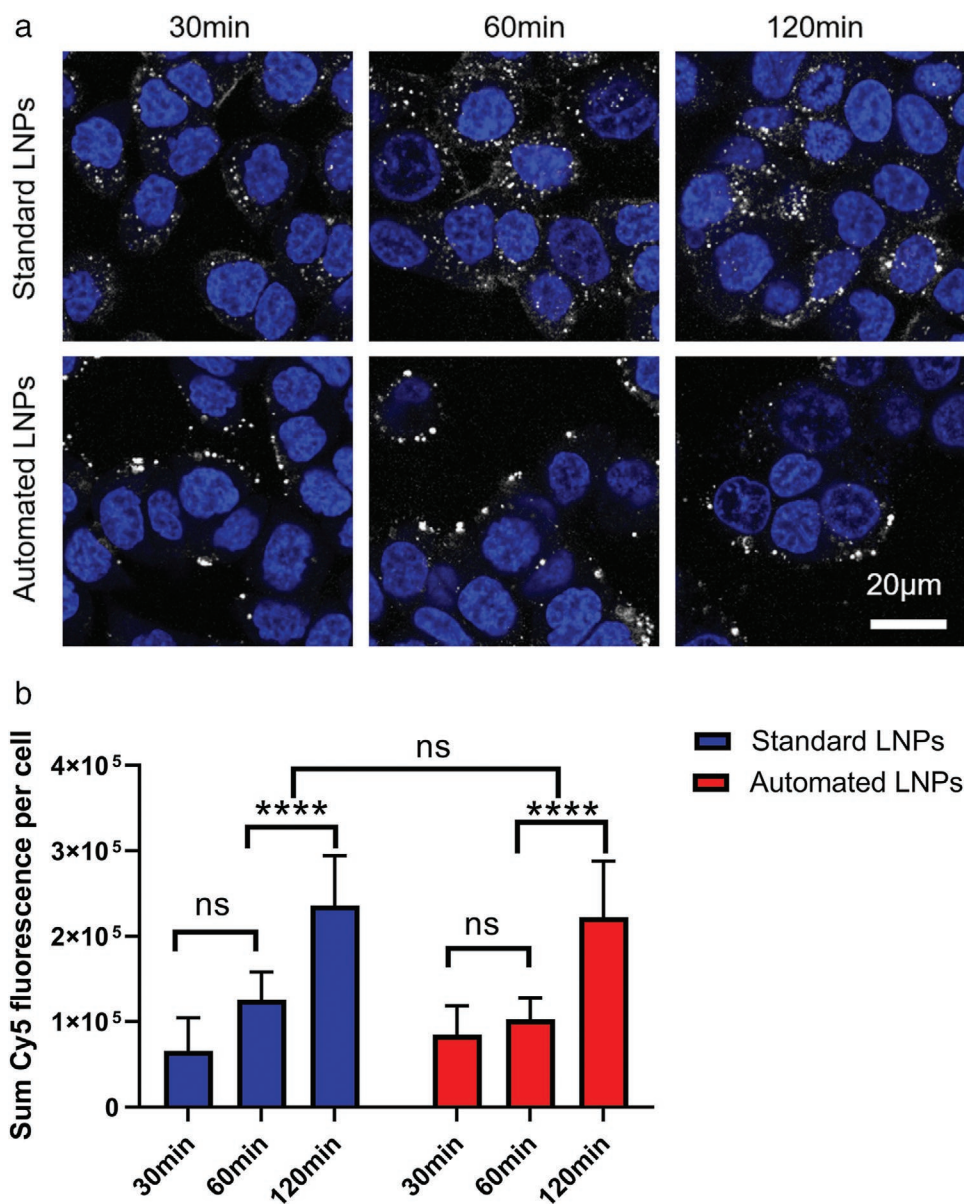
Figure 4. Cellular uptake of automated and standard Cy5-mRNA LNPs in H358 cells by confocal fluorescence microscopy. a) Cellular uptake images showing nuclei (Hoechst); Cy5-mRNA (white puncta); and its quantification at b) 30, 60, and 120 min. Two-way ANOVA analysis followed by Tukey's multiple comparison, **** $p < 0.0001$.

taken-up within the first 30 min and the uptake persisted at 60 min (Figure 4a,b). At 120 min, the cellular uptake was shown to increase for both LNP formulations (Figure 4b).

Another interesting finding was that standard mRNA LNPs exist in small puncta found throughout the cytoplasm, including close to the nucleus (Figure 4a). When the fluid-phase marker 10 kDa dextran (labeled with Oregon Green) was added to the incubation media, we observed mRNA LNPs within dextran-positive puncta, indicating that both standard and automated mRNA LNPs are taken into cells by either endosomes or macropinosomes (Figure S3, Supporting Information). It is reported that maturing endosomes move from the periphery to the center of the cells.[42] Therefore, the endosomes closer to the nucleus for the standard mRNA LNPs

are more likely to be acidified late endosomes or lysosomes. In contrast, the automated mRNA LNPs are seen in many large puncta, mostly at the cell periphery (Figure 4a). These localization differences are visible from the first time point (30 min) and persist to the last time point (120 min). We hypothesize that these large puncta are most likely the membrane-bound structures of macropinosomes. The size of endocytic vesicles has been used for macropinosome identification and applied in the study of macropinosome formation.[43,44] The size cut-off for clathrin-coated endosomal vesicles has been reported to be ≈85–100 nm[45,46] and macropinosomes ≈0.2–5 μm.[43,44,47] Given the large size of the automated mRNA LNPs, it is likely they are located within macropinosomes, as their diameter is much larger than that of clathrin-coated endosomes.
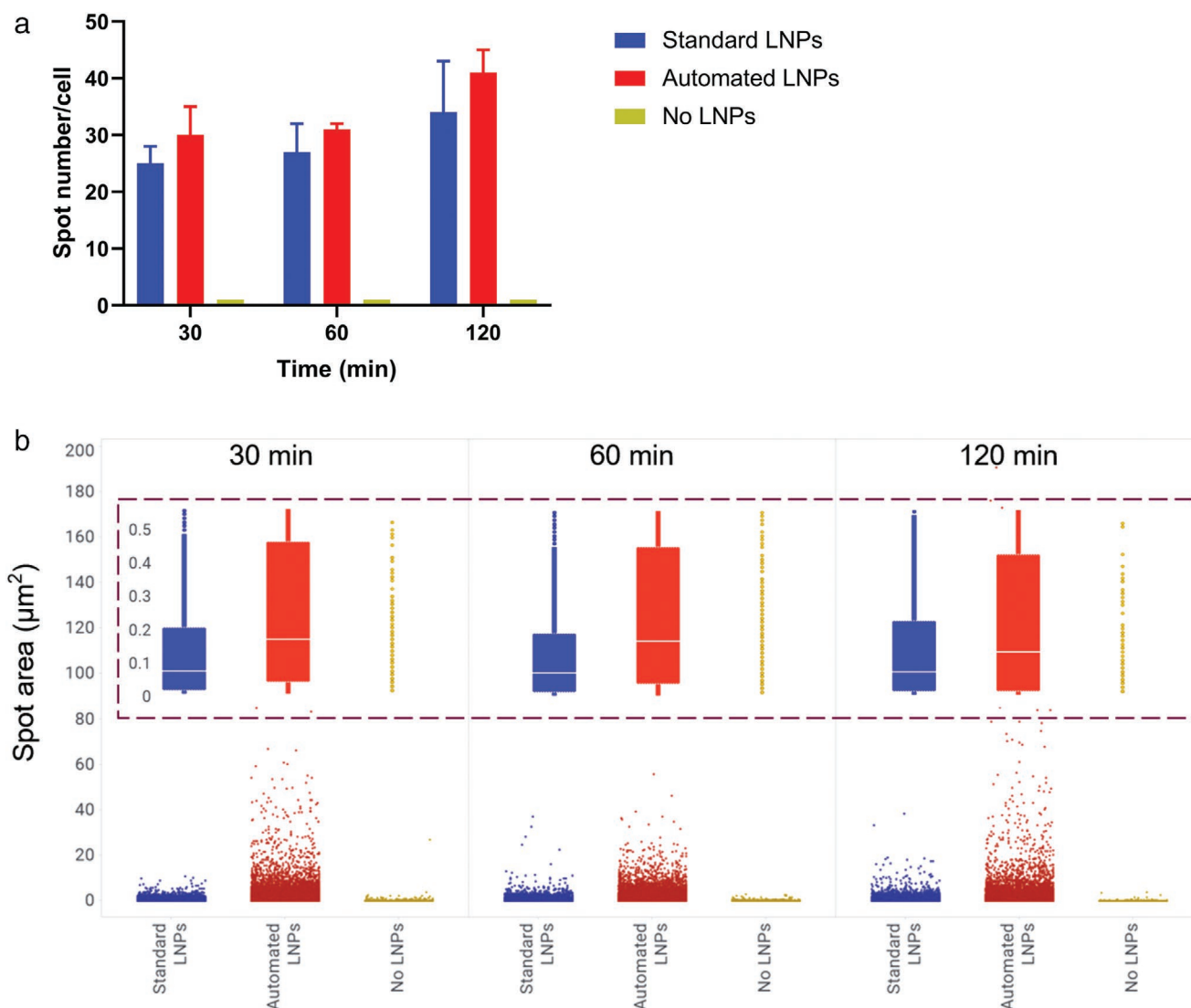
Figure 5. Automated mRNA LNP treated cells containing endocytic vesicles with larger diameter over 30–120 min. a) Spot number of Cy5-positive endocytic vesicles per cell (not statistically significant for the two LNP groups). b) Distribution of the spot area measurements. Insert shows corresponding median spot area.

To confirm the above hypothesis, we measured the number and size of Cy5-containing endocytic vesicles in each microscopy image. As shown in **Figure 5**a, the automated mRNA LNPs tend to have slightly more Cy5 spots than the standard mRNA LNPs over 30–120 min although the difference was not statistically significant. Figure 5b shows the size distribution of all the spots. Generally automated mRNA LNPs had a wider distribution of spot sizes at various time points, which is in line with the heterogeneous size distribution of macropinosomes.[47] The insert in Figure 5b shows the median spot area. As expected, the automated mRNA LNPs had a larger spot area than the standard mRNA LNPs, consistent with our hypothesis that these mRNA LNPs are found in macropinosomes. We hypothesize that the spot size for the standard mRNA LNPs was larger than that of an early clathrin-coated endosome because these endosomes can merge into larger sorting endosomes or late endosomes within 30-min,[43,47] which is our earliest data

point. The average spot areas did not change after 30 min for either LNP formulation, probably because early endocytic vesicles had already matured and reached an equilibrium state at 30 min. In line with this, Wang et al. have reported that within 5 min, macropinosomes can fuse with late endosomes and acquire endo-lysosomal markers after formation in HEK293 cells.[43] Kerr et al. reported that macropinosomes mature within 5–20 min.[47] **Table 3** summarizes the spot area and the resultant spot size assuming they are spherical. Indeed, the automated mRNA LNPs had a larger spot diameter (473 nm) than standard mRNA LNPs (323 nm), consistent with the macropinosome-biased uptake pathway of the automated mRNA LNPs.

Next, mRNA expression was measured in the presence of ethylisopropylamiloride (EIPA) and Pitstop2 to further investigate which endocytic pathways were involved in the intracellular uptake of the standard and automated mRNA LNPs. EIPA is an ion channel inhibitor of the Na+/H+ antiporter family,

Table 3. Summary of spot area and diameter at different time points.

Time	mRNA LNPs	Median spot area [μm²]	Approximate diameter [nm]
30 min	Standard	0.082	323
	Automated	0.176	473
	No treatment	0.012	123
60 min	Standard	0.082	323
	Automated	0.176	473
	No treatment	0.012	123
120 min	Standard	0.082	323
	Automated	0.141	424
	No treatment	0.012	123

which can specifically inhibit macropinocytosis.[20,48–51] Pitstop2 is an inhibitor for clathrin and can inhibit clathrin-dependent endocytosis.[52] As both of these treatments cause toxicity, we used the highest drug concentration which did not reduce cell confluency by more than 20% in order to avoid any interference from changes in cell density. As shown in **Figure 6**, mRNA expression for the standard LNPs was inhibited by 40% by Pitstop2. This observation indicates that the standard LNPs were taken up by a clathrin-mediated endocytic pathway, consistent with the earlier Cy5-mRNA cellular uptake data. Interestingly, incubation with EIPA also reduced by ≈50% the mRNA functional delivery of the standard LNPs, suggesting that the macropinocytosis pathway is also active in the cells treated with the standard LNPs.

The presence of both cellular uptake pathways for the standard mRNA LNPs is in line with their small particle size which allows the LNPs to fit into both endocytic vesicles. More interestingly, mRNA expression of the automated LNPs was inhibited by EIPA (50% inhibition) but not Pitstop2 ($p < 0.0001$). Indeed, these results indicate that it is macropinocytosis which primarily drives the cellular uptake of the automated mRNA LNPs and contributes to the enhanced mRNA functional delivery.

In summary, the total amount of mRNA taken into the cells does not appear to be significantly different between the standard and automated LNPs over 2 h of incubation. However,
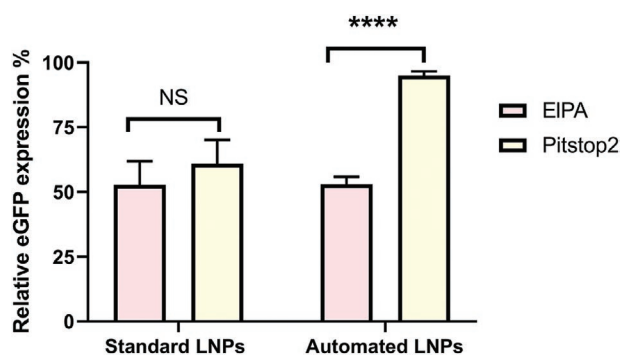
the automated LNPs appear to be internalized by the macropinosomal pathway (50% inhibition by EIPA but no inhibition by Pitstop2). This is consistent with our previous study, which also demonstrated that MC3-LNPs which target macropinocytosis exhibited an improved mRNA delivery in vitro and in vivo.[38] Other recent studies have revealed macropinosomal uptake as a productive pathway for LNP functional delivery.[20,50,53] One possible mechanism is that the macropinocytosis pathway reduces the amount of LNPs removed from the cells via recycling endosomes.[53] Alternatively, macropinosomes may acidify and fuse with lysosomes at a different and more favorable rate than early endosomes, thereby allowing more endosomal escape to occur before degradation[50,53,54] and/or have a more beneficial effect on the activation of mTOR pathway.[55,56] Macropinocytosis plays an essential role for amino acid-dependent activation of mTORC1.[57,58] Recent studies have demonstrated that mTOR also senses the presence of phosphatidic acid,[59,60] which enhances mTOR signaling by stabilizing mTOR complex.[59,61] Since phosphatidic acid is commonly hydrolyzed from phosphatidyl choline (PC), it is possible that the enriched DSPC on our automated LNPs can induce mTOR signaling and enhanced mRNA delivery. Patel et al. have demonstrated that manipulating mTOR can increase or inhibit mRNA LNP functional delivery and lipid-like molecules can improve mRNA LNP delivery.[56]

2.5. Protonation and Membrane Fusion of Automated mRNA LNPs

The response of LNPs to changes in pH is critical to their endosomal escape when being translocated through endocytic vesicles, and thereby allowing mRNA expression in cytosol. We investigated the pH response of the two types of mRNA LNPs by looking into protonation and hemolysis in acidic buffer conditions. **Figure 7**a shows the protonation profile of mRNA LNPs as a function of pH (pH range 3.5–11) as detected by the fluorescent dye TNS, which fluoresces upon binding to the protonated LNPs. As expected, in the basic buffer conditions, no protonation was observed. As the pH decreased from neutral (pH 7) to acidic (pH 5), both mRNA LNPs were rapidly protonated as shown by instant increase in relative fluorescence, followed by a plateau phase. From the sigmoidal protonation curve, an apparent pKa, defined as the pH at which 50% protonation is achieved, can be extrapolated.[32] pKa is a critical property of LNPs and it is reported to be correlated with mRNA expression.[62] The standard mRNA LNPs have a pKa of 6.31, consistent with other reports.[32] A similar pKa value of 6.24 was also determined for the automated mRNA LNPs, despite their different hydrodynamic sizes and surface properties.

Figure 7b shows the membrane fusion of the two mRNA LNPs when incubated with red blood cells (RBCs) in different pH conditions (7.5–4.5). RBCs have been used as model membranes to study endosomal escape mediated by LNPs and the results are indicative of intracellular mRNA and siRNA delivery.[17,63] Additionally, hemolysis that occurs in neutral pH conditions indicates a potential safety concern. In the present study, this rupture behavior of RBCs in acidic conditions
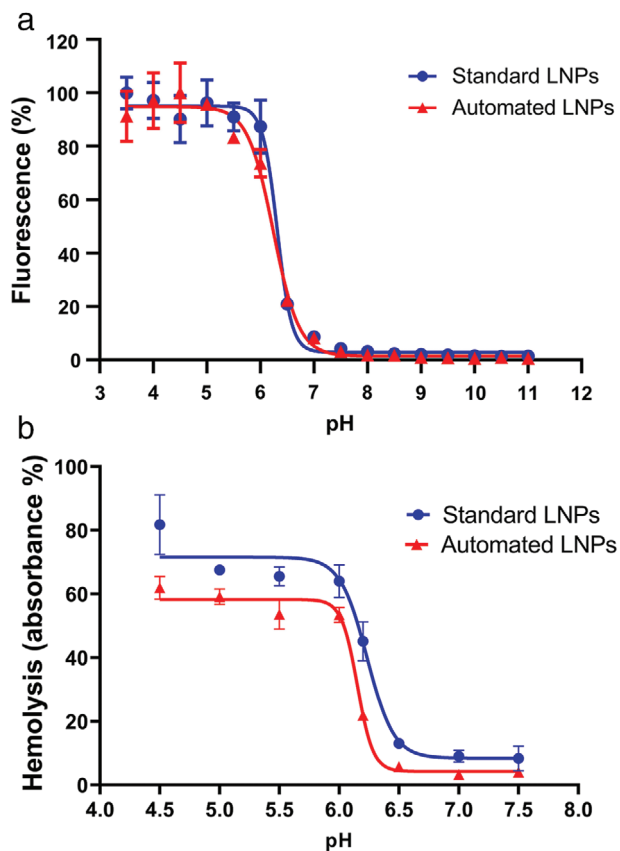

Figure 6. LNP eGFP mRNA expression in the presence of uptake inhibitors EIPA and Pitstop2 in H358 cells (24 h incubation, 10 μм) compared to vehicle-treated controls (100%). Analyzed by *t*-test. **** *p* < 0.0001.

**ADVANCED
SCIENCE NEWS**
www.advancedsciencenews.com

NANO · MICRO
small
www.small-journal.com

Figure 7. The response of eGFP mRNA LNPs to various pH conditions. a) Protonation and pKa measurement by TNS assay ($n = 3$). b) LNP-mediated hemolysis as evaluated by membrane fusion with RBCs (measured by UV absorbance of hemoglobin released from RBCs) ($n = 5$).

mimics endosomal perturbation and therefore predicts endosomal release induced by mRNA LNPs. As shown in Figure 7b, between neutral pH 7.5 and pH 6.5, both automated mRNA LNPs and standard mRNA LNPs had very low levels of hemolysis (≈5% and ≈10%, respectively). This indicates that both formulations could be tolerated upon delivery to the blood stream. However, the automated mRNA LNPs exhibit lower hemolysis than the standard mRNA LNPs at all pH values, suggesting greater biocompatibility with RBCs. For both mRNA LNPs, rapid hemolysis occurs at the pH ranging from 6.5 to 6.0 which matches well with early endosomal pH.[64] The hemolysis leveled off at pH > 6.5 for both mRNA LNPs. The hemolysis curves were fitted using a sigmoidal model, allowing us to calculate the pH at which 50% hemolysis is achieved, represented as pH (50% hemolysis). Interestingly, both mRNA LNPs have similar pH (50% hemolysis) of 6.23 versus 6.15. Besides pH (50% hemolysis), the hemolysis rate at pH (50% hemolysis) was fitted (as Hill slope) to evaluate how fast mRNA LNPs-induced hemolysis occurs. Interestingly, the rate of the hemolysis induced by the automated mRNA LNPs was much faster than the standard mRNA LNPs (6.531 vs 3.863). This indicates that the automated mRNA LNPs are more disruptive and can rapidly escape endosomes than the standard mRNA LNPs, which could partly account for the enhanced mRNA functional delivery.

2.6. Enhanced mRNA Functional Delivery of Automated LNPs is Translated In Vivo

We next investigated whether the higher mRNA in vitro expression mediated by automated LNPs can be reproduced in vivo. LNPs were loaded with Fluc mRNA, allowing us to detect translated luciferase protein via its enzymatic activity, which is production of photons from luciferin substrate. The mRNA-encapsulated automated LNPs and standard LNPs were then dosed to mice via tail vein injection as a head-to-head comparison.

Figure 8a shows whole body bioluminescence images of mice after injection of both mRNA LNPs (6 and 24-h time points). The intensity of bioluminescence is reflective of the amount of luciferase protein that has been translated in vivo. We observed strong Fluc mRNA expression for both LNPs, as shown by bright bioluminescence radiance (Figure 8a). There is no detectable bioluminescence in the PBS-treated control group. Reflecting what we had observed in vitro, the luminescence intensity of the automated mRNA LNP group was significantly higher than the standard mRNA LNP group. The quantification data in Figure 8b showed a 4.5-fold improvement in luciferase signal at the 6-h time point. More importantly, the enhanced mRNA expression by the automated LNPs was maintained at 24 h, although the global bioluminescence decreased.

To compare mRNA LNP biodistribution, the main organs of mice were taken out at the 24-h post administration and were imaged as shown in Figure 8c. As expected, the liver showed the greatest mRNA expression, followed by the spleen. Interestingly, the automated LNP groups exhibited 5.4-fold higher mRNA expression in liver than the standard LNPs (Figure 8d), consistent with the whole body imaging results. Therefore, we conclude that the increased mRNA functional delivery by the automated LNPs is translated from in vitro to in vivo.

It is worthwhile noting that we also observed mRNA expression in the inguinal white adipose tissue (iWAT) and gonadal white adipose tissue (gWAT) with the automated LNPs, but not with the standard mRNA LNPs. In addition, we found some bioluminescence signal in the injection site of the mouse tail (two of three mice for both 6 and 24-h post injection) for the automated LNP groups but no bioluminescence for all mice in the standard LNP or PBS groups. This indicates that the automated mRNA LNPs had local functional delivery of mRNA. Together, we can conclude that these mRNA LNPs have the potential to target non-liver tissues, which can be achieved by manipulating LNP physicochemical properties. Indeed, other tissues such as lung or spleen are being explored to be specifically targeted by altering the properties of LNPs.[9,65]

2.7. Enhanced mRNA Functional Delivery of Automated LNPs is Related to Their Size

To further investigate the underlying mechanism of improved in vivo mRNA functional delivery of the automated LNPs, we prepared another group of standard mRNA LNPs (termed: standard LNPs large). These mRNA LNPs were prepared using the same standard microfluidics method, however, some process parameters were adjusted to obtain LNPs with sizes
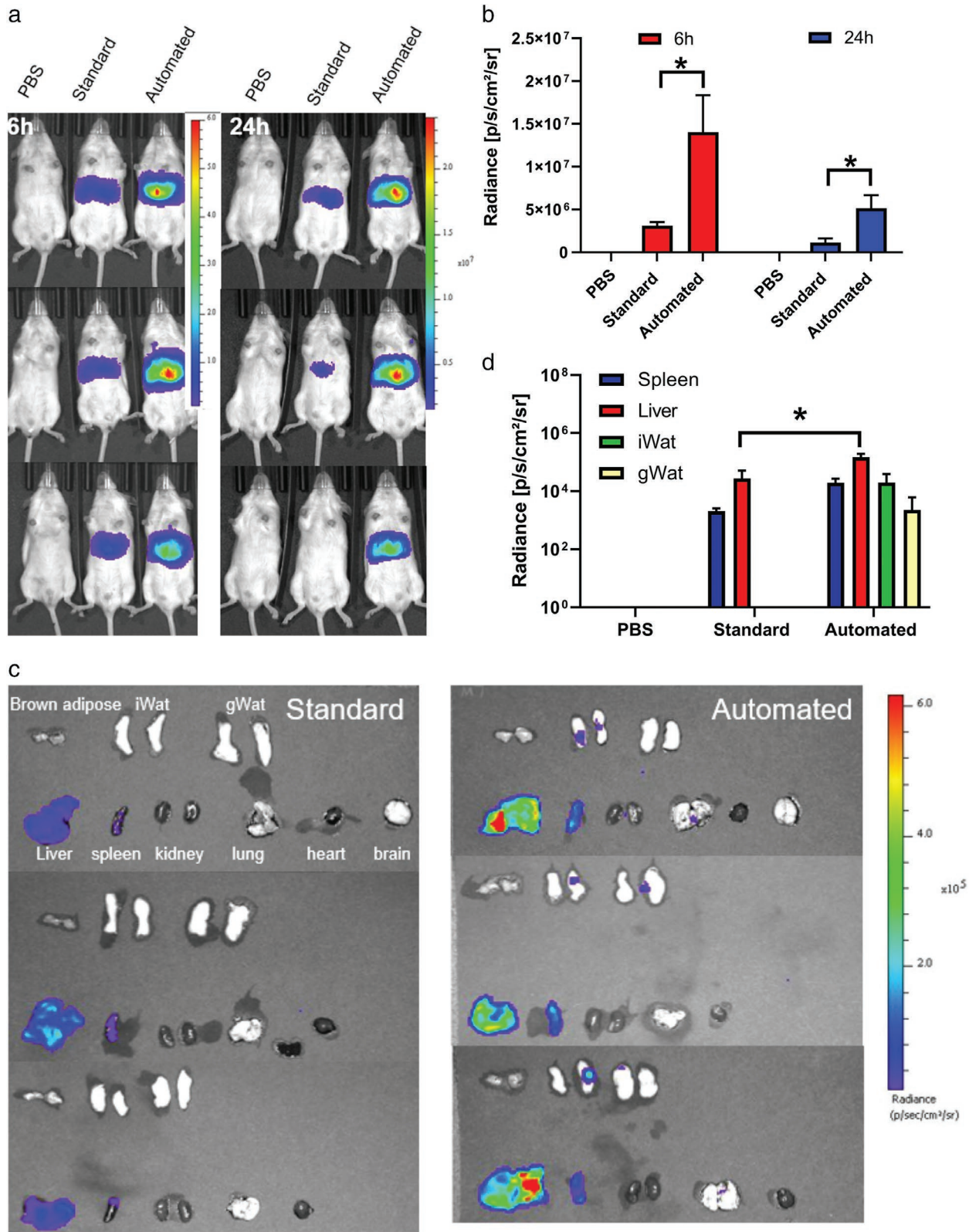
Figure 8. In vivo functional delivery of automated LNPs compared with standard LNPs encapsulating mRNA encoding luciferase. Mice ($n = 3$) were dosed at 0.25 mg per kg via tail vein i.v. injection and luminescence was imaged by IVIS. a) Whole body luminescence imaging at 6 and 24 h post injection. b) Quantification of whole body imaging. c) Ex vivo organ luminescence imaging at 24-h post injection. d) Quantificaiton of ex vivo organ imaging. T-test. *$p < 0.05$.

ADVANCED
SCIENCE NEWS
www.advancedsciencenews.com

NANO · MICRO
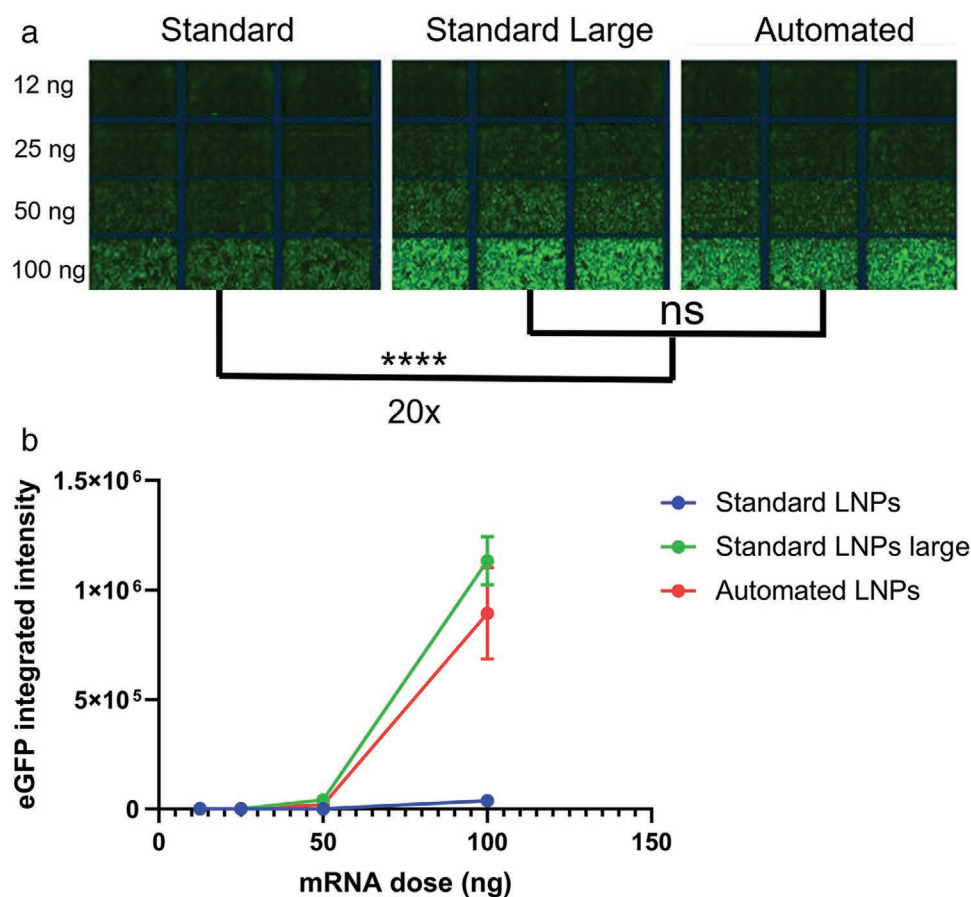small
www.small-journal.com

Figure 9. Effect of LNP size on the eGFP mRNA functional delivery in H358 cells. a) eGFP fluorescence images; b) quantification of eGFP mRNA expression. *T*-test. **** $p < 0.0001$.

comparable to the automated LNPs (120 nm, PDI 0.138). This was to ensure all LNP formulations had the same compositions and ratios and thus, an unbiased-comparison of mRNA expression in cells could be performed. We hypothesized that the larger size of LNPs is associated with enhanced mRNA functional delivery based on our observations that automated LNPs were larger and had more mRNA copies per particle (Tables 1 and 2, and Figure 3). As shown in **Figure 9**, the automated mRNA LNPs were more potent than the standard mRNA LNPs, as we had observed before ($p < 0.0001$). Interestingly, the "standard LNPs large" rendered a 20-fold higher mRNA expression than the normal standard LNPs, which shows that the mRNA expression can be improved by increasing the size of the LNPs. More importantly, the automated LNPs and the "standard LNPs large" displayed comparable levels of mRNA expression, once again suggesting that LNP size is a key determinant of LNP biological activity. The positive effect of LNP particle size on mRNA functional delivery is also supported by the observation that mRNA expression in vitro was increased when LNP size increased from 50 to 130 nm.[29,66] Next, these three LNP formulations were intravenously injected into mice and we found that the automated LNPs and the "standard LNPs large" showed the same Fluc mRNA expression, which was more potent than the normal standard LNPs (3.2-fold) (partial unpublished data), revealing that the positive effect from larger

mRNA LNPs can be reproduced in mice.[38] The particle size of mRNA LNP vaccines that are below 150 nm was also observed to have an enhancing effect on mouse immunogenicity via intramuscular administration.[67]

Overall, these results indicate that large LNPs are a valuable approach to enhancing mRNA functional delivery. It is reported that small LNPs (50–150 nm) are more potent for siRNA delivery than larger LNPs (>150 nm).[68,69] However, mRNA molecules are much larger than siRNA molecules (at least 50-fold longer in terms of nucleotides). Our findings show that increasing particle size is favorable for loading more mRNA copies per LNP, which is reasonably correlated with the number of mRNA released into the cytosol assuming the same number of nanoparticles escape from endosomes. In summary, our mechanistic study reveals that the pharmaceutical properties of LNPs need to be tuned and optimized when developing LNPs for the delivery of longer RNAs.

2.8. Corona Protein Profiling of Automated mRNA LNPs

LNPs are intrinsically fatty and hydrophobic particles. They adsorb serum proteins to form a corona when they are in contact with blood. It is well-established that the protein corona formed at the surface of LNPs has an impact on their biological

fate.[33,70] In this study, we investigated the protein corona bound to the three mRNA LNPs ("standard LNPs", "standard LNPs large," and "automated LNPs") to assess the relative protein abundance and whether a relationship with size could be detected.

Again, all mRNA LNPs had the same composition with differences in size only. All mRNA LNP formulations were first incubated with fresh serum collected from mice, then the mRNA LNPs with protein coronas were extracted, digested, and analyzed with mass spectrometry (MS). The overall number of protein species was determined by MS/MS sequencing. As expected, the overall number of identified proteins was similar for all three formulations (≈380 species, Figure S4a, Supporting Information) and all three mRNA LNPs had a similar protein richness distribution (Figure S4b, Supporting Information).

The overall protein species were further categorized for each formulation in **Figure 10**a. The vast majority (349) of the corona proteins was identified in all three LNP formulations, consistent with other studies.[71] Although the corona protein species largely overlapped, the intensity of each protein was varied. Among the identified corona proteins, we looked specifically at the apolipoproteins due to their reported association with LNP functionality.[33] The clustering analysis of the protein intensity was performed with the K-means method to illustrate the similarity of the three types of coronas. As shown in Figure 10b, the coronas for the automated mRNA LNPs and the standard large mRNA LNPs showed a higher similarity in terms of protein abundance. Figure 10c shows the relative protein abundance (RPA%) of each apolipoprotein in the three formulations. Among all the apolipoproteins, ApoE, ApoC3, ApoD, and ApoA (1,2,4) were found to be enriched in all the mRNA LNPs. Interestingly, ApoE is the most abundant (28–30%) apolipoprotein, consistent with the reported theory of ApoE being the endogenous ligand for LNP liver tropism.[33] Also, the observed ApoE binding is in line with the neutral surface of these LNPs (Table 1). It was reported that only neutral LNPs bind to ApoE and target liver, rather than highly negative or positive LNPs or liposomes.[33,72]

Figure 10d shows specifically the abundance of ApoE in the corona. Interestingly, the two large mRNA LNPs have the same percentage of ApoE content (30%), significantly higher than small mRNA LNPs (28%, $p < 0.01$), which reveals that large size is associated with ApoE binding. From a physicochemical perspective, ApoE binding is consistent with the hydrophobic surface of large mRNA LNPs. Classical LNPs utilizing MC3 as an ionizable lipid were reported to function in an ApoE- and low-density lipoprotein receptor (LDLR)-dependent way.[33] Our standard mRNA LNPs have been shown to be ApoE-dependent and could be dependent on LDLR for uptake because the size of the standard mRNA LNPs is closer to the size of LDL particles (20–30 nm).[73] Furthermore, LDLR-dependent uptake is consistent with the dominant endocytosis uptake pathway of the standard mRNA LNPs (Figures 5–7) in H358 cells which have been profiled to express LDLR.[74] In contrast, the standard large mRNA LNPs and the automated mRNA LNPs are expected to be taken up via an LDLR-independent pathway in vivo since the size is too large to fit inside the endocytic vesicles which internalize LDLR (clathrin-mediated endosomes). This hypothesis is supported by the fact that large LNPs were taken up mainly via macropinocytosis pathway in vitro (Figures 5–7). It is worth noting that ApoE-dependency is not contradictory with LDLR-independency. ApoE is not just a component of LDL but also a part of VLDL (very low density lipoprotein) and HDL (high density lipoprotein), therefore could mediate uptake via receptors related with VLDL and HDL.[75] Similar to our findings, lipidoid LNPs have been shown to be ApoE-dependent but LDLR-independent, and the major uptake pathway is macropinocytosis.[51,76] Further in vivo studies are needed to study whether LDLR is involved in the cellular uptake of the automated mRNA LNPs.

In summary, we have characterized the automated mRNA LNPs together with the standard mRNA LNPs in order to extract the key physicochemical properties that contribute to the improved biological activities. As summarized in **Figure 11**, the automated mRNA LNPs show greater mRNA expression in vitro and in vivo and are found to contain more mRNA per particle, have a larger size, more DSPC on the surface, and are more hemolytic. All these properties are associated and influence mRNA LNP cellular uptake, intracellular fate, and biological activities. Most importantly, we have identified that mRNA loading per particle is a key parameter to ensure sufficient mRNA to be delivered into the cytosol for protein expression. Unveiling the critical mRNA loading property has a significant implication for the design of mRNA delivery systems with greater delivery efficiency and higher therapeutic index.
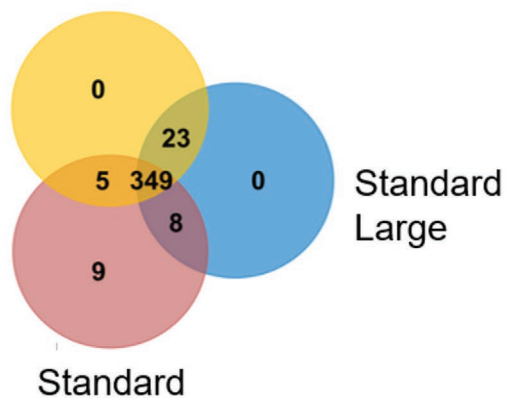
3. Conclusion

We demonstrated that the MC3 LNPs prepared from the previously established high-throughput platform showed enhanced mRNA activity in vivo, although the purpose of establishing this platform was for in vitro screening rather than for in vivo application. The mechanistic investigation reveals mRNA loading per nanoparticles is critical for mRNA functional delivery. Large LNPs tend to have high mRNA loading per particle, more hydrophobic surface, and more hemolytic and beneficial cellular uptake pathways. These identified pharmaceutical and biological properties can be correlated with the improved mRNA functional delivery in vitro and in vivo. We believe that our findings will accelerate research and development of mRNA therapeutics or vaccines by defining critical quality attributes for LNP-mediated mRNA delivery. This study emphasizes the importance of understanding the relationship of physicochemical properties with biological activities, and the optimization of pharmaceutical properties when developing formulations for new nucleic acid modalities.
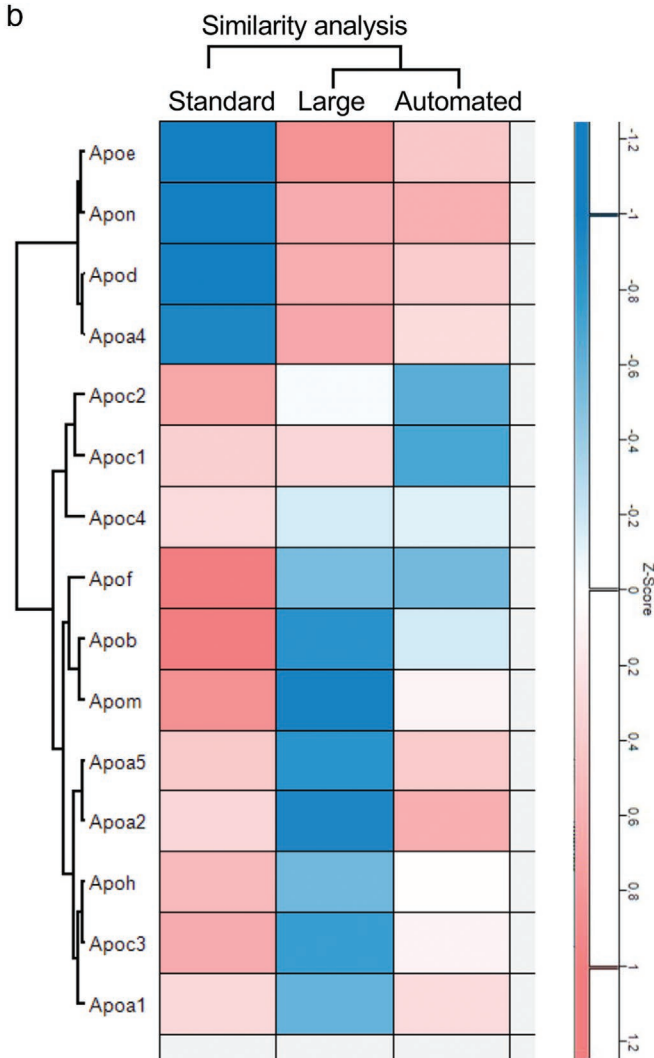
4. Experimental Section

Materials: The ionizable cationic lipid O-(*Z,Z,Z,Z*-heptatriaconta-6,9,26,29-tetraem-19-yl)-4-(*N,N*-dimethylamino)butanoate (DLin-MC3-DMA) was synthesized at AstraZeneca. The 1,2-distearoyl-sn-glycero-3-phosphocholine (DSPC) was obtained from Avanti Polar Lipids; 1,2-Dimyristoyl-rac-glycero-3-methylpolyoxyethylene-2000 (DMG-PEG2000) was obtained from NOF Corporation; and cholesterol (Chol) was obtained from Sigma–Aldrich. Deuterated DSPC (d83) and Chol (d7) were obtained from Avanti Polar Lipids. eGFP, Cyanine-5 eGFP (Cy5 eGFP)
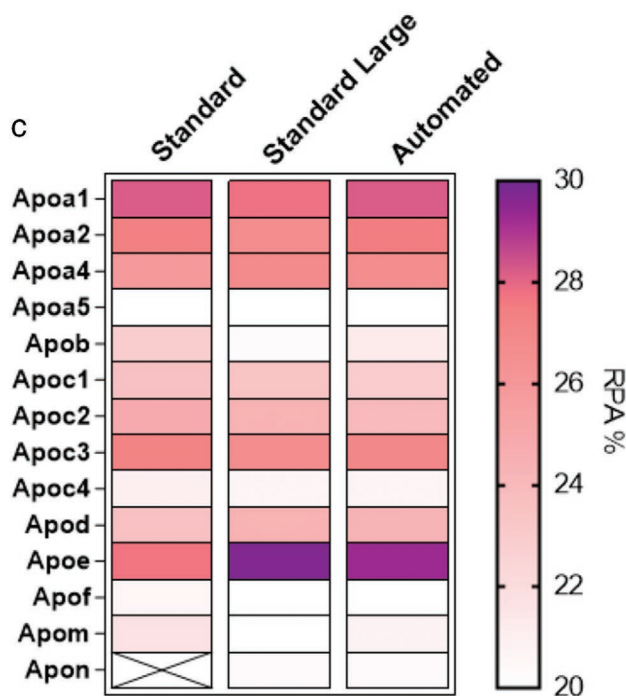
ADVANCED
SCIENCE NEWS

www.advancedsciencenews.com
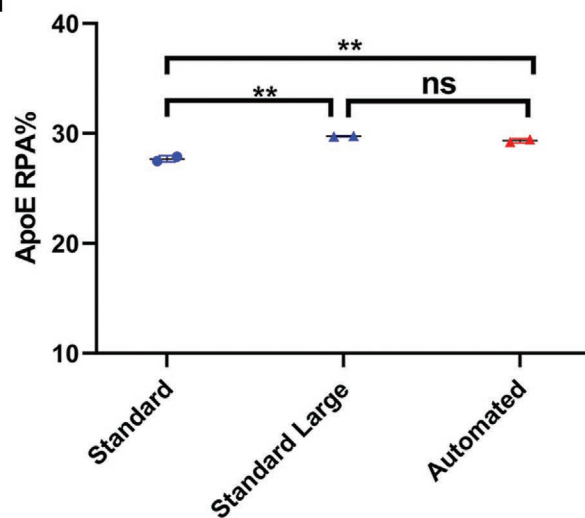
NANO · MICRO

small

www.small-journal.com

Figure 10. The protein corona coating of Fluc mRNA LNP nanoparticles when incubated with mouse plasma. a) Categorization of absorbed protein species. b) Abundance of apolipoprotein is normalized by Z-scoring. Similarity of the three coronas was compared using clustering analysis. c) Absorbed lipoprotein content shown as relative protein abundance (RPA%). d) Comparison of ApoE abundance. One-way ANOVA followed by multiple comparisons, $**p < 0.01$. Two biological repeats were performed for all LNP protein corona processes and analysis.
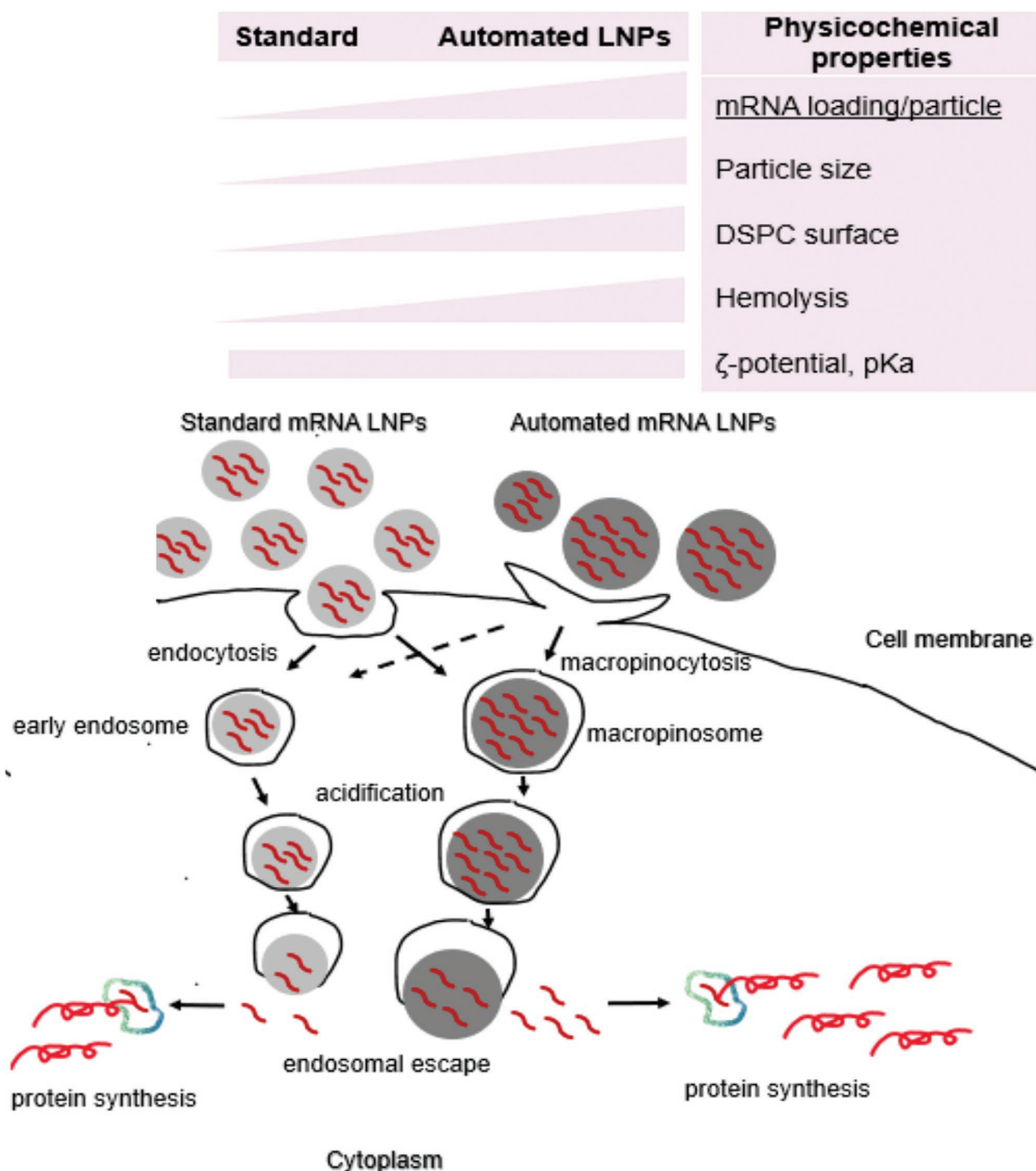
Figure 11. A summary of the main difference characterized for the standard and the automated mRNA LNPs and the proposed mechanism of the resultant mRNA transfection. Triangle indicates an increasing trend whereas bar shows no variation. The automated mRNA LNPs follow a macropinocytosis-biased uptake pathway leading to more mRNA being delivered to the cytosol of the target cell for protein expression.

mRNA (996 nucleotides), and Fluc mRNA (1929 nucleotides) Cleancap capped and modified with 5-methoxyuridine were purchased from TriLink Biotechnologies. D2O was obtained from Sigma–Aldrich. Citrate buffer was purchased from Teknova, and RNase free water for molecular biology was obtained from Sigma–Aldrich. (2-(p-toluidinyl)naphthalene-6-sulfonic acid (TNS)) (in sodium salt) was purchased from Sigma–Aldrich.

LNP Preparations: Both standard and automated MC3 LNPs were made of the same lipids and compositions (MC3:DSPC:cholesterol:DMG-PEG2k, 50:10:38.5:1.5 molar ratio) and were prepared as previously described.[29] In short, Nanoassemblr (Precision Nanosystems) and Hamilton liquid handling system (Microlab STAR) were used to prepare LNPs at three volumetric portions of mRNA to 1 volumetric

portion of lipid solutions (mRNA: lipids 1:20 weight ratio) to obtain a lipid concentration of 2.81 mg mL^{-1} (4.80 mм). The clean-up of the crude formulations was achieved by dialysis in PBS using Slide-A-Lyzer G2 dialysis cassettes (Thermo Scientific, MWCO 10 K) or 96 well microdialysis membrane (Thermo Scientific Pierce, MWCO 10 K). mRNA encapsulation efficiency (EE%), defined as encapsulated mRNA relative to overall mRNA including free and encapsulated mRNA, was quantified by Quant-it Ribogreen Assay Kit (Thermo Fisher Scientific) according to manufacturer's instructions. The hydrodynamic ζ-size and surface ζ-potential of LNPs were measured in a Nano ZS Zetasizer (Malvern-Panalytics) at a back scattering angle of 173 °C.

TNS Assay: The pKa of eGFP mRNA LNPs was measured using the TNS assay.[77] The buffers (10 mм sodium acetate or phosphate and 150 mм sodium chloride) used in the assay were titrated to pH values varying from 3.5 to 11 in 96-well plates. The final concentration of the LNPs and TNS diluted into these buffers were 25 and 6 µм, respectively. Fluorescence intensity was read on a fluorescence plate reader (Envision, Perkin Elmer) using excitation and emission of 323 and 435 nm, respectively. Fluorescence was normalizedto 100% for maximum fluorescence readings. The apparent pKa was calculated as the pH corresponding to 50% LNP protonation as fitted using non-linear sigmoidal dose-response (variable slope, GraphPad Prism 8).

Hemolysis Assay: The hemolysis assay was used to measure the LNP capability to escape from endosomes. The assay was tested in the pH range of 4.5 to 7.5, using buffers with 0.5 pH unit difference. The buffers were 10 mм strength and 150 mм NaCl for isotonicity. Buffers between 4.5 and 5.5 were sodium acetate and between 6 and 7.5 were sodium phosphate. Fresh rat red blood cells stabilized with Alsever's, were purchased from Envigo and used within one week of pooling. Fresh eGFP mRNA LNP samples were diluted in PBS to obtain the same mRNA concentration (1.6 µg mL^{-1}). A solution of Triton X, 10% in PBS, was used as positive control. Red blood cells (RBCs, counted by hemocytometer C-Chip Labtech) were initially diluted with PBS to obtain 1×10^9 cells per mL concentration. Cells were pelleted by centrifuging for 5 min at 500 g, resuspended in PBS, and washed to remove all the stabilizer. RBCs were then divided into equal volumes in the number of vials corresponding to the pHs to test, pelleted again, and resuspended with the required volume and the desired pH buffer. The assay was carried out in sterile 96-well clear polystyrene microplates (Corning). For each pH condition, 150 µL of RBCs solution was added to every well and then, 4 µL of samples in 5 repeats including positive (Triton X) and negative (buffer) controls. The plates were incubated at room temperature for 90 min before readout. The plates were then centrifuged for 5 min at 500 g and 100 µL of the supernatant transfer to clear Nunc MicroWell 96-well microplates (Thermo Fisher) and absorbance measured at 450 nm. Data were analyzed by subtracting the absorbance of the vehicle (PBS) control and plot as %hemoglobin released compared to Triton X-treated samples (100%). The results were fit in GraphPad-Prism 8.0 with non-linear fit sigmoidal dose-response (variable slope).

CryoTEM: CryoTEM images were captured as a service of FEI at the Nanoscience Centre, University of Cambridge. Both eGFP mRNA LNPs were blotted on carbon coated-copper grids (300 mesh, 2 mm, Quantifoil R1.2/1.3), then snap-frozen in liquid ethane using a VitrobotMKIV equipment. The grids were glow discharged in a Pelco Easiglo glow discharge unit for 60 s at 25 mA and under 0.39 mbar vacuum. Both LNPs (2 µL, 1 mg mL^{-1} mRNA) were double blotted for 2.5 s using Vitrobot (4 °C, 100% relative humidity). The blotting force was calibrated to give a "wedge" of thick ice on roughly 1/3 of the grids and a gradient ice thickness on the other 2/3 of the grids. The vitrified LNPs were stored in liquid nitrogen. Images were acquired on a Titan KriosTM G3i TEM (FEI, Thermo Scientific) equipped with a Falcon 3 direct detector using the single particle data acquisition package EPU (1.10). Scale bar and contrast were processed in Fiji (Image J).

SANS: Small-angle neutron scattering (SANS) measurements on lipid nanoparticles were performed on the Sans2d beamline at the ISIS Neutron and Muon source (STFC, Rutherford-Appleton Laboratory, Didcot, U.K.). The eGFP mRNA LNP samples were measured at 0.3 mg mL^{-1} of mRNA which corresponds to a lipid concentration of 6 mg mL^{-1}

with 27% D_2O PBS buffer, in quartz cells of 1 mm pathlength, and at room temperature. The scattering from samples and buffer was recorded on two 1 m^2 2D detectors positioned 5 and 12 m from the sample, using neutrons of wavelengths, λ, in the range 1.75–12.5 Å, and giving a scattering vector ($Q = 4\pi sin\theta/\lambda$, where $\theta/2$ is the scattering angle) in the range $0.0016 \leq Q \leq 0.5$ Å^{-1}. The 2D isotropic scattering raw data were corrected for the efficiency and spatial linearity of the detectors, sample transmissions and path length, and backgrounds arising from the instrument and cells, and then radially-averaged to 1D and transformed to scattering cross-section using the Mantid framework (https://www.mantidproject.org/). The data were then put on an absolute scale using the scattering from a standard sample (comprising a solid blend of protiated and perdeuterated polystyrene) measured with the same instrument configuration in accordance with established procedures.[78]

SAXS: Small-angle X-ray and Wide-angle X-ray scattering (SAXS and WAXS) measurements were performed on a Nano-inXider instrument (Xenocs, Sassenage, France) at the Materials Characterization Laboratory of the ISIS Neutron and Muon source (STFC, Rutherford-Appleton Laboratory, Didcot, U.K.). The setup used a micro-focus sealed-tube Cu 30W/30 µm X-ray source (Cu K-α, $\lambda = 1.54$ Å). The SAXS and WAXS (covering the respective Q ranges of 0.0045 to 0.37 Å^{-1} and 0.3 to 4.1 Å^{-1}) were detected simultaneously using two Dectris Pilatus 3 hybrid pixel detectors. Scattering from the samples and the PBS buffer was collected in 1-mm glass capillaries at room temperature. Data reduction (azimuthal averaging, buffer subtraction, absolute scaling) was carried out using the Foxtrot software.

Small-Angle Scattering Data Analysis: The analyses of the SANS and SAXS data were performed using the SANS analysis package from NIST with Igor Pro.[79] The lipid composition across the LNPs was determined using the sample with the lipid molar composition DLin-MC3-DMA:DSPC:Chol:DMG-PEG2000 of 50:10:38.5:1.5, where deuterated DSPC ($C_{44}D_{83}NO_8P$) and cholesterol ($C_{27}H_{39}D_7O$) were used. SANS and SAXS data were complementary to each other to illustrate the structure information. The SANS/SAXS data was fitted using a polydisperse core with N shells model that describes the form factor of a core with two shells structure, where the core has a specific radius and polydispersity. The SLD of the core and each shell were individually specified. The fitting was performed while fixing as many of the SLD values as possible. The starting SLD values of the core and shells were calculated from the input formulation molar ratio of each component assuming MC3/cholesterol and DSPC/DMG-EPG are mainly distributed in the core and in the shell, respectively and fitted within the SLD ranges of the components. Solvents were calculated with the input compositions. In order to compare the structural difference between two LNP preparation methods, SAXS and SANS data obtained from the same LNPs were first fitted separately to obtain the initial range of the parameters. Then, both SANS and SAXS data were fitted simultaneously using the global fitting method. The core size and polydispersity, and the thickness of two shells were linked and the main parameters to fit were the core radius, polydispersity, and the SLDs for both core and shells. Fitting the automated LNP with the core size close to that obtained from DLS measurement was unsuccessful.

Cell Culture: Human lung epithelial (NCI-H358) and human hepatocellular carcinoma (HepG2) were obtained from American type culture collection (ATCC). Human embryonic kidney 293 cells with traffic light reporter (HEK293T TLR) were obtained internally/a proprietary cell line from AstraZeneca. H358 cells were cultured in RPMI 1640 (Gibco, Thermo Fisher) supplemented with 10% fetal bovine serum (FBS) (Gibco, Thermo Fisher), 2 mм GlutaMAX (Gibco, Thermo Fisher) (growth media). HepG2 cells were cultured in medium essential medium (MEM) (Gibco, Thermo Fisher) supplemented with 10% FBS. HEK293T TLR cells were cultured in Dulbecco's modified eagle medium (DMEM) (Gibco, Thermo Fisher) supplemented with 10% FBS. Cells were maintained in a humidified 5% CO_2 atmosphere at 37 °C for up to ten passages and were regularly tested for mycoplasma (MycoSEQ, ThermoFisher).

mRNA LNP Transfection: One day prior to transfection, 4.0×10^3 cells per well were seeded in 30 µL of complete cell culture media into

ADVANCED
SCIENCE NEWS
www.advancedsciencenews.com

NANO · MICRO
small
www.small-journal.com

poly-D-lysine black clear-bottom 384-well plates (Greiner). For confocal microscopy experiments, cells were seeded in CellCarrier Ultra 384-well plates at 15 000 cells per well. The following day, LNPs containing 12.5–50 ng of mRNA (eGFP/mCherry) were added into cells followed by the addition of 20 µL of complete cell culture media using the acoustic droplet dispenser ECHO 550 (Labcyte). The cells were imaged using an Incucyte S3 (Essen Bioscience) and mRNA expression was monitored using a 10× objective every 4 h for a total of 48 h. The acquired images were analyzed using the integrated Incucyte S3 2019A software. Statistical analysis was performed using t-test, one-way, or two-way ANOVA in GraphPad Prism 8.

mRNA LNP Endocytosis Assays: In order to measure LNP uptake, H358 cells were incubated with LNP containing Cy5-labelled mRNA at a final mRNA concentration of 1 µg mL^{-1} (50 ng per well) and Hoechst 33 342 in complete cell culture media for 30, 60, or 120 min at 37 °C. LNPs-containing medium was then removed, cells were washed twice using PBS, and returned to fresh cell culture media in room temperature. Cells were imaged immediately at room temperature, to limit continued intracellular trafficking, on a Yokogawa CV8000 automated confocal microscope, using a 60× water-immersion objective (numerical aperture 1.2). Maximum projection images were collected for 10 Z planes, 1 µm apart, to capture the full depth of the cells.

To determine colocalization of LNPs with 10 and 70 kDa dextran, cells were treated with LNP and Hoechst as above, and also with 50 µg mL^{-1} dextran labeled with Oregon Green (Thermo Scientific). Live samples were imaged on a Yokogawa CV8000 automated confocal microscope, using a 60× water-immersion objective (numerical aperture 1.2) at one Z plane. Images were analyzed for cell number and whole cell fluorescence intensity measurements using Columbus (version 2.8.2 and 2.8.3, Perkin Elmer), and spot number and size measurements were performed using ImageJ/FIJI (version 1.53c).

Inhibition of eGFP mRNA LNP Expression: EIPA [5-(N-ethyl-N-isopropyl)amiloride] (Sigma–Aldrich) and Pitstop2 (Abcam) were used to assess the effects of inhibiting different internalization mechanisms on the productive delivery of mRNA. One day prior to transfection, 8.0×10^3 (H358) cells per well were seeded in 30 µL of growth culture media into poly-D-lysine black clear-bottom 384-well plates (Greiner) and incubated at 37 °C/5% CO$_2$. The following day, the inhibitors were added into cells at a final concentration of 10 µM using an ECHO 525 (Labcyte). After 1 h incubation with the endocytosis inhibitors at 37 °C/5% CO$_2$, LNPs containing 50 ng of mCherry mRNA per well to a final concentration of 40 ng µL^{-1} were added into cells using an ECHO 550 (Labcyte). Immediately after LNP addition, 20 µL of growth medium was added to each well and cells were imaged as described in the previous section. The confluence was monitored and maintained >80%. Statistical analysis was performed using t-test in GraphPad Prism 9.

Animals: Female BALB/c mice ≈6–8 weeks of age were obtained from Charles River, UK and were housed in the AstraZeneca animal facility (Babraham Research Campus). All procedures were carried out in accordance with the Home Office U.K. ethical and husbandry standards, under the authority of a project license of P8A7322E2.

IVIS Imaging: Mice were randomized and received tail injections of 100 µL of luciferase mRNA LNPs at a dose of 0.25 mg per kg. 6 and 24 h post injection, mice were injected with 0.1 mL (15 mg mL^{-1}) XenoLight D-Luciferin (Perkin Elmer) via i.p. route. Mice were anesthetized in a chamber with 3% isoflurane prior to imaging. 15 min post D-Luciferin administration, mice were imaged in an IVIS spectrum imager (Perkin Elmer) including organs (liver, spleen, lungs, kidneys, heart, brain, and fat tissues such as brown and white adiposes) exercised at 24 h. Bioluminescence was quantified as average radiance (p s^{-1} cm^{-2} sr^{-1}) and the data analyzed with GraphPad Prism v8.1.1 using t-test (significant p value <0.05).

Protein Corona Extraction: Protein corona study was performed as previously established.[80] First, Fluc mRNA LNPs were incubated in 10% mouse plasma harvested from the in vivo animals at 1 µg mL^{-1} of mRNA (equivalent to 50 ng dose for imaging analysis) for 4 h (37 °C) to form stable corona. Anti-PEG [PEG-2-128] (Abcam) antibodies were crosslinked to the surface of Dynabeads M-270 Epoxy (Thermo Fisher

Scientific) to separate the corona-LNPs complexes from the free plasma. The LNP pull-down quantification was obtained from particle numbers acquired from nanoparticle tracking analysis. For mass spectrometry, sample preparation was performed on an equal amount of recovered LNPs. Briefly, sample denaturation and reduction were done in one step using urea and Bond-Breaker TCEP solution (Thermo Fisher Scientific), followed by alkylation using 2-chloroacetamide. Protein digestion was performed overnight in trypsin and ceased by the addition of formic acid. Each digest was loaded into C18 trap column Evotip (Evosep) according to manufacturer's instruction.

Proteomics Analysis: Corona proteins were quantified using a Q-Exactive HF orbitrap mass spectrometer (Thermo Fisher Scientific) coupled with an Evosep One (Evosep) sample loader. Protein digests containing Evotips were loaded onto Evosep One sample loader for peptide desalting and purification immediately prior to analytical column separation (Waters). Purified peptides were then separated at a 0.5 µL min^{-1} flow rate on the analytical column (C18, 8cm, Evosep) with gradient offset focusing to achieve a 3–40% acetonitrile gradient within a 44 min loop.

Raw spectra obtained were analyzed by MaxQuant software (version 1.6.6.0) with cysteine carbamidomethylation as a fixed modification and N-terminal acetylation and methionine oxidations as variable modifications. The false discovery rate (determined by a decoy database) was set to 1% for both proteins and peptides with a minimum length of seven amino acids. Enzyme specificity was set to trypsin as protease, and a maximum of two missed cleavages were allowed. Protein identification was then searched against the mouse Uniprot database (version June 2019). Quantification was performed with a minimum ratio count of 1. To obtain a complete description of the pattern of mean differences among the conditions, an ANOVA comparison was performed on biological and technical replicates. Bioinformatics analyses were performed with the Perseus software (version 1.6.2.3). Protein relative abundances were computed using intensity based absolute quantification (iBAQ) values (protein content, intensity% relative to total identified corona protein).The iBAQ is a sum of all identified peptide intensities divided by the number of peptides and is approximately proportional to the number of moles of proteins present. For significant analysis of ApoE contents of three formulations, unpaired t-test was performed using Prism. For heatmap clustering analysis, a z-score was used to describe similarity of protein corona formed on each LNP formulation. The z-score represents distance away from the mean (in the unit of standard deviation). In the heatmap clustering analysis, a false discovery rate of 5% in multiple sample testing was applied.

Supporting Information

Acknowledgements

Conflict of Interest

The authors declare the following financial interests: L. Cui, S. Sonzini, S. Pereira, W. Li, L. Liang, B. Yang and A. S. Desai are employed by AstraZeneca R&D Cambridge during the development of this work.

Author Contributions

L.C., M.R.H., S.Z., S.P., K.L., S.M.R., L.L., N.M., and A.S.D. designed and performed the experiments. B.Y and W.L. simulated SANS and SAXS data. L.C. wrote the manuscript with support from all authors and edits from M.R.H., S.M.R., S.P., and N.M. All authors have given approval to the final version of the manuscript.

Data Availability Statement

The data that support the findings of this study are available from the corresponding author upon reasonable request.

Keywords

[1] W. Wang, Y. Li, Y. Wang, C. Shi, C. Li, Q. Li, R. J. Linhardt, *Biotechnol. Adv.* **2018**, *36*, 2129.

[2] H. Steinle, A. Behring, C. Schlensak, H. P. Wendel, M. Avci-Adali, *Stem Cells* **2017**, *35*, 68.

[3] N. Pardi, M. J. Hogan, F. W. Porter, D. Weissman, *Nat. Rev. Drug Discovery* **2018**, *17*, 261.

[4] P. S. Kowalski, A. Rudra, L. Miao, D. G. Anderson, *Mol. Ther.* **2019**, *27*, 710.

[5] WHO, "Draft landscape of COVID-19 candidate vaccines," **2020**.

[6] A. Mullard, *Nat. Rev. Drug Discovery* **2020**, *19*, 367.

[7] L. M. Kranz, M. Diken, H. Haas, S. Kreiter, C. Loquai, K. C. Reuter, M. Meng, D. Fritz, F. Vascotto, H. Hefesha, C. Grunwitz, M. Vormehr, Y. Hüsemann, A. Selmi, A. N. Kuhn, J. Buck, E. Derhovanessian, R. Rae, S. Attig, J. Diekmann, R. A. Jabulowsky, S. Heesch, J. Hassel, P. Langguth, S. Grabbe, C. Huber, Ö. Türeci, U. Sahin, *Nature* **2016**, *534*, 396.

[8] V. Anttila, A. Saraste, J. Knuuti, P. Jaakkola, M. Hedman, S. Svedlund, M. Lagerström-Fermér, M. Kjaer, A. Jeppsson, L. M. Gan, *Mol. Ther. – Methods Clin. Dev.* **2020**, *18*, 464.

[9] Q. Cheng, T. Wei, L. Farbiak, L. T. Johnson, S. A. Dilliard, D. J. Siegwart, *Nat. Nanotechnol.* **2020**, *15*, 313.

[10] J. D. Finn, A. R. Smith, M. C. Patel, L. Shaw, M. R. Youniss, J. van Heteren, T. Dirstine, C. Ciullo, R. Lescarbeau, J. Seitzer, R. R. Shah, A. Shah, D. Ling, J. Growe, M. Pink, E. Rohde, K. M. Wood, W. E. Salomon, W. F. Harrington, C. Dombrowski, W. R. Strapps, Y. Chang, D. V. Morrissey, *Cell Rep.* **2018**, *22*, 2227.

[11] K. Karikó, J. M. Keller, V. A. Harris, D. J. Langer, F. A. Welsh, *J. Neurosci. Methods* **2001**, *105*, 77.

[12] D. M. Mauger, B. J. Cabral, V. Presnyak, S. V. Su, D. W. Reid, B. Goodman, K. Link, N. Khatwani, J. Reynders, M. J. Moore, I. J. McFadyen, *Proc. Natl. Acad. Sci. U.S.A.* **2019**, *116*, 24075.

[13] B. K. Muralidhara, R. Baid, S. M. Bishop, M. Huang, W. Wang, S. Nema, *Drug Discovery Today* **2016**, *21*, 430.

[14] Q. Chen, Y. Zhang, H. Yin, *Adv. Drug Delivery Rev.* **2021**, *168*, 246.

[15] K. Karikó, H. Muramatsu, F. A. Welsh, J. Ludwig, H. Kato, S. Akira, D. Weissman, *Mol. Ther.* **2008**, *16*, 1833.

[16] J. Nelson, E. W. Sorensen, S. Mintri, A. E. Rabideau, W. Zheng, G. Besin, N. Khatwani, S. V. Su, E. J. Miracco, W. J. Issa, S. Hoge, M. G. Stanton, J. L. Joyal, *Sci. Adv.* **2020**, *6*, eaaz6893.

[17] S. Liu, Q. Cheng, T. Wei, X. Yu, L. T. Johnson, L. Farbiak, D. J. Siegwart, *Nat. Mater.* **2021**, *20*, 701.

[18] L. Miao, L. Li, Y. Huang, D. Delcassian, J. Chahal, J. Han, Y. Shi, K. Sadtler, W. Gao, J. Lin, J. C. Doloff, R. Langer, D. G. Anderson, *Nat. Biotechnol.* **2019**, *37*, 1174.

[19] J. A. Kulkarni, P. R. Cullis, R. van der Meel, *Nucleic Acid Ther.* **2018**, *28*, 146.

[20] J. Gilleron, W. Querbes, A. Zeigerer, A. Borodovsky, G. Marsico, U. Schubert, K. Manygoats, S. Seifert, C. Andree, M. Stöter, H. Epstein-Barash, L. Zhang, V. Kotelyansky, K. Fitzgerald, E. Fava, M. Bickle, Y. Kalaidzidis, A. Akinc, M. Maier, M. Zerial, *Nat. Biotechnol.* **2013**, *31*, 638.

[21] P. R. Cullis, M. J. Hope, *Mol. Ther.* **2017**, *25*, 1467.

[22] S. C. Semple, A. Akinc, J. Chen, A. P. Sandhu, B. L. Mui, C. K. Cho, D. W. Y. Sah, D. Stebbing, E. J. Crosley, E. Yaworski, I. M. Hafez, J. R. Dorkin, J. Qin, K. Lam, K. G. Rajeev, K. F. Wong, L. B. Jeffs, L. Nechev, M. L. Eisenhardt, M. Jayaraman, M. A. Maier, M. Srinivasulu, M. J. Weinstein, Q. Chen, R. Alvarez, S. A. Barros, S. De, S. K. Klimuk, T. Borland, *Nat. Biotechnol.* **2010**, *28*, 172.

[23] M. A. Maier, M. Jayaraman, S. Matsuda, J. Liu, S. Barros, W. Querbes, Y. K. Tam, S. M. Ansell, V. Kumar, J. Qin, X. Zhang, Q. Wang, S. Panesar, R. Hutabarat, M. Carioto, J. Hettinger, P. Kandasamy, D. Butler, K. G. Rajeev, B. Pang, K. Charisse, K. Fitzgerald, B. L. Mui, X. Du, P. Cullis, T. D. Madden, M. J. Hope, M. Manoharan, A. Akinc, *Mol. Ther.* **2013**, *21*, 1570.

[24] V. L. M. Herrera, A. H. Colby, N. Ruiz-Opazo, D. G. Coleman, M. W. Grinstaff, *Nanomedicine* **2018**, *13*, 2083.

[25] A. Akinc, A. Zumbuehl, M. Goldberg, E. S. Leshchiner, V. Busini, N. Hossain, S. A. Bacallado, D. N. Nguyen, J. Fuller, R. Alvarez, A. Borodovsky, T. Borland, R. Constien, A. De Fougerolles, J. R. Dorkin, K. Narayanannair Jayaprakash, M. Jayaraman, M. John, V. Kotelyansky, M. Manoharan, L. Nechev, Q. Qin, T. Racie, D. Raitcheva, K. G. Rajeev, D. W. Y. Sah, J. Soutschek, I. Toudjarska, H. P. Vornlocher, T. S. Zimmermann, et al., *Nat. Biotechnol.* **2008**, *26*, 561.

[26] K. T. Love, K. P. Mahon, C. G. Levins, K. A. Whitehead, W. Querbes, J. R. Dorkin, J. Qin, W. Cantley, L. L. Qin, T. Racie, M. Frank-Kamenetsky, K. N. Yip, R. Alvarez, D. W. Y. Sah, A. de Fougerolles, K. Fitzgerald, V. Kotelyansky, A. Akinc, R. Langer, D. G. Anderson, *Proc. Natl. Acad. Sci. USA* **2010**, *107*, 1864.

[27] M. A. Maier, M. Jayaraman, S. Matsuda, J. Liu, S. Barros, W. Querbes, Y. K. Tam, S. M. Ansell, V. Kumar, J. Qin, X. Zhang, Q. Wang, S. Panesar, R. Hutabarat, M. Carioto, J. Hettinger, P. Kandasamy, D. Butler, K. G. Rajeev, B. Pang, K. Charisse, K. Fitzgerald, B. L. Mui, X. Du, P. Cullis, T. D. Madden, M. J. Hope, M. Manoharan, A. Akinc, *Mol. Ther.* **2013**, *21*, 1570.

[28] A. K. K. Leung, Y. Y. C. Tam, S. Chen, I. M. Hafez, P. R. Cullis, *J. Phys. Chem. B* **2015**, *119*, 8698.

[29] M. Yanez Arteta, T. Kjellman, S. Bartesaghi, S. Wallin, X. Wu, A. J. Kvist, A. Dabkowska, N. Székely, A. Radulescu, J. Bergenholtz, L. Lindfors, *Proc. Natl. Acad. Sci. U.S.A.* **2018**, *115*, E3351.

[30] J. A. Kulkarni, M. M. Darjuan, J. E. Mercer, S. Chen, R. van der Meel, J. L. Thewalt, Y. Y. C. Tam, P. R. Cullis, *ACS Nano* **2018**, *12*, 4787.

[31] Y. Eygeris, S. Patel, A. Jozic, G. Sahay, *Nano Lett.* **2020**, *20*, 4543.

[32] M. Jayaraman, S. M. Ansell, B. L. Mui, Y. K. Tam, J. Chen, X. Du, D. Butler, L. Eltepu, S. Matsuda, J. K. Narayanannair, K. G. Rajeev, I. M. Hafez, A. Akinc, M. A. Maier, M. A. Tracy, P. R. Cullis, T. D. Madden, M. Manoharan, M. J. Hope, *Angew. Chem., Int. Ed.* **2012**, *51*, 8529.

[33] A. Akinc, W. Querbes, S. De, J. Qin, M. Frank-Kamenetsky, K. N. Jayaprakash, M. Jayaraman, K. G. Rajeev, W. L. Cantley, J. R. Dorkin, J. S. Butler, L. Qin, T. Racie, A. Sprague, E. Fava, A. Zeigerer, M. J. Hope, M. Zerial, D. W. Sah, K. Fitzgerald, M. A. Tracy, M. Manoharan, V. Kotelyansky, A. De Fougerolles, M. A. Maier, *Mol. Ther.* **2010**, *18*, 1357.

[34] L. Cui, S. Pereira, S. Sonzini, S. van Pelt, S. M. Romanelli, L. Liang, D. Ulkoski, V. R. Krishnamurthy, E. Brannigan, C. Brankin, A. S. Desai, unpublished.

[35] K. J. Hassett, K. E. Benenato, E. Jacquinet, A. Lee, A. Woods, O. Yuzhakov, S. Himansu, J. Deterling, B. M. Geilich, T. Ketova, C. Mihai, A. Lynn, I. McFadyen, M. J. Moore, J. J. Senn, M. G. Stanton, Ö. Almarsson, G. Ciaramella, L. A. Brito, *Mol. Ther. – Nucleic Acids* **2019**, *15*, 1.

[36] H. Wood, *Nat. Rev. Neurol.* **2018**, *14*, 570.

[37] T. Wei, Q. Cheng, Y. L. Min, E. N. Olson, D. J. Siegwart, *Nat. Commun.* **2020**, *11*, 3232.

[38] M. R. Hunter, L. Cui, T. B. Porebski, S. Pereira, S. Sonzini, U. Odunze, P. Iyer, O. Engkvist, R. L. Lloyd, S. Peel, A. Sabirsh, D. Ross-Thriepland, A. T. Jones, A. S. Desai, unpublished.

[39] S. A. Pillai, D. Chobisa, D. Urimi, N. Ravindra, *J. Pharm. Sci. Res.* **2016**, *8*, 271.

[40] K. J. Kauffman, J. R. Dorkin, J. H. Yang, M. W. Heartlein, F. Derosa, F. F. Mir, O. S. Fenton, D. G. Anderson, *Nano Lett.* **2015**, *15*, 7300.

[41] F. Sebastiani, M. Yanez Arteta, M. Lerche, L. Porcar, C. Lang, R. A. Bragg, C. S. Elmore, V. R. Krishnamurthy, R. A. Russell, T. Darwish, H. Pichler, S. Waldie, M. Moulin, M. Haertlein, V. T. Forsyth, L. Lindfors, M. Cárdenas, *ACS Nano* **2021**, *15*, 6709.

[42] J. Huotari, A. Helenius, *EMBO J.* **2011**, *30*, 3481.

[43] J. T. H. Wang, R. D. Teasdale, D. Liebl, *MethodsX* **2014**, *1*, 36.

[44] J. T. H. Wang, M. C. Kerr, S. Karunaratne, A. Jeanes, A. S. Yap, R. D. Teasdale, *PLoS One* **2010**, *5*, e13763.

[45] H. T. McMahon, E. Boucrot, *Nat. Rev. Mol. Cell Biol.* **2011**, *12*, 517.

[46] G. P. Vigers, R. A. Crowther, B. M. Pearse, *EMBO J.* **1986**, *5*, 2079.

[47] M. C. Kerr, R. D. Teasdale, *Traffic* **2009**, *10*, 364.

[48] H. P. Lin, B. Singla, P. Ghoshal, J. L. Faulkner, M. Cherian-Shaw, P. M. O'Connor, J. X. She, E. J. Belin de Chantemele, G. Csányi, *Br. J. Pharmacol.* **2018**, *175*, 3640.

[49] M. A. Islam, Y. Xu, W. Tao, J. M. Ubellacker, M. Lim, D. Aum, G. Y. Lee, K. Zhou, H. Zope, M. Yu, W. Cao, J. T. Oswald, M. Dinarvand, M. Mahmoudi, R. Langer, P. W. Kantoff, O. C. Farokhzad, B. R. Zetter, J. Shi, *Nat. Biomed. Eng.* **2018**, *2*, 850.

[50] K. T. Love, K. P. Mahon, C. G. Levins, K. A. Whitehead, W. Querbes, J. R. Dorkin, J. Qin, W. Cantley, L. L. Qin, T. Racie, M. Frank-Kamenetsky, K. N. Yip, R. Alvarez, D. W. Y. Sah, A. De Fougerolles, K. Fitzgerald, V. Koteliansky, A. Akinc, R. Langer, D. G. Anderson, *Proc. Natl. Acad. Sci. U.S.A.* **2010**, *107*, 1864.

[51] Y. Dong, K. T. Love, J. R. Dorkin, S. Sirirungruang, Y. Zhang, D. Chen, R. L. Bogorad, H. Yin, Y. Chen, A. J. Vegas, C. A. Alabi, G. Sahay, K. T. Olejnik, W. Wang, A. Schroeder, A. K. R. Lytton-Jean, D. J. Siegwart, A. Akinc, C. Barnes, S. A. Barros, M. Carioto, K. Fitzgerald, J. Hettinger, V. Kumar, T. I. Novobrantseva, J. Qin, W. Querbes, V. Koteliansky, R. Langer, D. G. Anderson, *Proc. Natl. Acad. Sci. U.S.A.* **2014**, *111*, 3955.

[52] L. Von Kleist, W. Stahlschmidt, H. Bulut, K. Gromova, D. Puchkov, M. J. Robertson, K. A. MacGregor, N. Tomlin, A. Pechstein, N. Chau, M. Chircop, J. Sakoff, J. P. Von Kries, W. Saenger, H. G. Kräusslich, O. Shupliakov, P. J. Robinson, A. McCluskey, V. Haucke, *Cell* **2011**, *146*, 471.

[53] G. Sahay, W. Querbes, C. Alabi, A. Eltoukhy, S. Sarkar, C. Zurenko, E. Karagiannis, K. Love, D. Chen, R. Zoncu, Y. Buganim, A. Schroeder, R. Langer, D. G. Anderson, *Nat. Biotechnol.* **2013**, *31*, 653.

[54] M. Hamasaki, N. Araki, T. Hatae, *Anat. Rec.* **2004**, *277*, 298.

[55] Y.-X. Li, H.-B. Pang, *J. Controlled Release* **2020**, *329*, 1222.

[56] S. Patel, G. Sahay, *Nano Lett.* **2017**, *17*, 5711.

[57] S. Yoshida, R. Pacitto, K. Inoki, J. Swanson, *Cell. Mol. Life Sci.* **2018**, *75*, 1227.

[58] M. Laplante, D. M. Sabatini, *Curr. Biol.* **2009**, *19*, R1046.

[59] D. Menon, D. Salloum, E. Bernfeld, E. Gorodetsky, A. Akselrod, M. A. Frias, J. Sudderth, P. H. Chen, R. DeBerardinis, D. A. Foster, *J. Biol. Chem.* **2017**, *292*, 6303.

[60] D. A. Foster, *Trends Endocrinol. Metab.* **2013**, *24*, 272.

[61] J. M. Joy, D. M. Gundermann, R. P. Lowery, R. Jäger, S. A. McCleary, M. Purpura, M. D. Roberts, S. M. C. Wilson, T. A. Hornberger, J. M. Wilson, *Nutr. Metab.* **2014**, *11*, 29.

[62] K. A. Hajj, R. L. Ball, S. B. Deluty, S. R. Singh, D. Strelkova, C. M. Knapp, K. A. Whitehead, *Small* **2019**, *15*, 1805097.

[63] C. A. Alabi, K. T. Love, G. Sahay, H. Yin, K. M. Luly, R. Langer, D. G. Anderson, *Proc. Natl. Acad. Sci. U.S.A.* **2013**, *110*, 12881.

[64] N. Demaurex, *News Physiol. Sci.* **2002**, *17*, 1.

[65] Q. Li, C. Chan, N. Peterson, R. N. Hanna, A. Alfaro, K. L. Allen, H. Wu, W. F. Dall'Acqua, M. J. Borrok, J. L. Santos, *ACS Chem. Biol.* **2020**, *15*, 830.

[66] M. J. Carrasco, S. Alishetty, M. Alameh, H. Said, L. Wright, M. Paige, O. Soliman, D. Weissman, T. E. C. Iv, A. Grishaev, M. D. Buschmann, *Commun. Biol.* **2021**, *4*, 956.

[67] K. J. Hassett, J. Higgins, A. Woods, B. Levy, Y. Xia, C. J. Hsiao, E. Acosta, Ö. Almarsson, M. J. Moore, L. A. Brito, *J. Controlled Release* **2021**, *335*, 237.

[68] A. Akinc, M. Goldberg, J. Qin, J. R. Dorkin, C. Gamba-Vitalo, M. Maier, K. N. Jayaprakash, M. Jayaraman, K. G. Rajeev, M. Manoharan, V. Koteliansky, I. Röhl, E. S. Leshchiner, R. Langer, D. G. Anderson, *Mol. Ther.* **2009**, *17*, 872.

[69] S. Chen, Y. Y. C. Tam, P. J. C. Lin, M. M. H. Sung, Y. K. Tam, P. R. Cullis, *J. Controlled Release* **2016**, *235*, 236.

[70] D. Chen, N. Parayath, S. Ganesh, W. Wang, M. M. Amiji, *Nanoscale* **2019**, *11*, 18806.

[71] S. Tenzer, D. Docter, J. Kuharev, A. Musyanovych, V. Fetz, R. Hecht, F. Schlenk, D. Fischer, K. Kiouptsi, C. Reinhardt, K. Landfester, H. Schild, M. Maskos, S. K. Knauer, R. H. Stauber, *Nat. Nanotechnol.* **2013**, *8*, 772.

[72] X. Yan, F. Kuipers, L. M. Havekes, R. Havinga, B. Dontje, K. Poelstra, G. L. Scherphof, J. A. A. M. Kamps, *Biochem. Biophys. Res. Commun.* **2005**, *328*, 57.

[73] H. Lodish, A. Berk, S. L. Zipursky, P. l. Matsudaira, D. Baltimore, J. Darnell, *Molecular Cell Biology*, 4th edition, W.H. Freeman & Co Ltd, New York **2000**.

[74] E. J. Sayers, S. E. Peel, A. Schantz, R. M. England, M. Beano, S. M. Bates, A. S. Desai, S. Puri, M. B. Ashford, A. T. Jones, *Mol. Ther.* **2019**, *27*, 1950.

[75] G. S. Getz, C. A. Reardon, *J. Lipid Res.* **2009**, *50*, S156.

[76] Y. Dong, K. T. Love, J. Robert Dorkin, S. Sirirungruang, Y. Zhang, D. Chen, R. L. Bogorad, H. Yin, Y. Chen, A. J. Vegas, C. A. Alabi, G. Sahay, K. T. Olejnik, W. Wang, A. Schroeder, A. K. R. Lytton-Jean, D. J. Siegwart, A. Akinc, C. Barnes, S. A. Barros, M. Carioto, K. Fitzgerald, J. Hettinger, V. Kumar, T. I. Novobrantseva, J. Qin, W. Querbes, V. Koteliansky, R. Langer, N. Tompkins, et al., *Proc. Natl. Acad. Sci. U.S.A.* **2014**, *111*, 3955.

[77] M. Jayaraman, S. M. Ansell, B. L. Mui, Y. K. Tam, J. Chen, X. Du, D. Butler, L. Eltepu, S. Matsuda, J. K. Narayanannair, K. G. Rajeev, I. M. Hafez, A. Akinc, M. A. Maier, M. A. Tracy, P. R. Cullis, T. D. Madden, M. Manoharan, M. J. Hope, *Angew. Chem., Int. Ed.* **2012**, *51*, 8529.

[78] G. D. Wignall, F. S. Bates, *J. Appl. Crystallogr.* **1987**, *20*, 28.

[79] S. R. Kline, *J. Appl. Crystallogr.* **2006**, *39*, 895.

[80] K. Liu, N. Ralf, E. Lázaro-Ibáñez, T. Miliotis, M. Lerche, R. S. Ribeiro, M. Strimfors, H. Duàn, J. Ulander, D. Lindén, A. Salvati, A. Sabirsh, **2021**, https://doi.org/10.21203/rs.3.rs-827883/v1.